https://doi.org/10.1016/j.tafmec.2021.103194

This is the Pre-Published Version.

A systematic 3D simulation method for geomaterials with block inclusions from image recognition to fracturing modelling

Yuexiang Lin[1], Zhen-Yu Yin[2], Xiang Wang[2*], Linchong Huang[1]

[1] Postdoctoral Fellow, College of Aeronautics and Astronautics, Sun Yat-Sen University, Shenzhen, China. Department of Civil and Environmental Engineering, The Hong Kong Polytechnic University, Hong Kong, China. Tel: +86 15111008697; Email:linyx86@mail.sysu.edu.cn

[2] Associate Professor, Department of Civil and Environmental Engineering, The Hong Kong Polytechnic University, Hong Kong, China. Tel: +852 3400 8470; Fax: +852 2334 6389; Email: zhenyu.yin@polyu.edu.hk

[3] Research assistant professor, Department of Civil and Environmental Engineering, The Hong Kong Polytechnic University, Hong Kong, China. Tel: +852 6993 1903; Email: xiang.wang@polyu.edu.hk

[4] Professor, College of Aeronautics and Astronautics, Sun Yat-Sen University, Shenzhen, China. Tel: +86 13926022266; Email:hlinch@mail.sysu.edu.cn

Abstract: A systematic hybrid modelling approach for heterogeneous geomaterials with irregular block inclusions is creatively developed based on a deep learning technique, computational geometry algorithms, and a 3D finite-discrete (or discrete-finite) element method; the approach includes the following three major steps: (1) the deep learning-based image identification technique and the computational geometry algorithm are employed to establish a 2D geometry library of realistic rock blocks; (2) 3D block inclusions with desired block shapes are regenerated by a surface morphing technique and then randomly allocated to the specimen domain based on the overlapping detection algorithm; and (3) the finite-discrete element method is developed by integrating cohesive elements with a solid mesh based on a finite element code to simulate the progressive fracture and interface behaviours of heterogeneous geomaterials. To validate the proposed hybrid approach, a series of synthetic specimens with Brazilian split tests are prepared and implemented from 2D to 3D. The results verified that the finite-discrete model can be easily established through images, and the consequent simulation performance is validated through comparisons between observations and numerical results regarding failure patterns and stress-strain relations. Using the calibrated and verified approach, we further numerically discuss the influence of the block-matrix strength ratio and interface strength on the mechanical responses of bimrocks. All results demonstrate that the proposed hybrid approach has a powerful ability to dealing with heterogeneous composite materials that maintain the characteristics of both continuity and discontinuity.

Keywords: Heterogeneous geomaterials; Realistic shapes; Hybrid finite-discrete element modelling; Fracture behaviour.

© 2021. This manuscript version is made available under the CC-BY-NC-ND 4.0 license http://creativecommons.org/licenses/by-nc-nd/4.0/.

1 Introduction

The mechanical responses of heterogeneous geomaterials with irregular block inclusions can be very complex and problematic (Shao et al., 2017, Li et al., 2019 and Li et al., 2020). Representatives include volcanic agglomerates, conglomerates, breccias, mélanges, and faulty or weathered rocks. The block inclusion features, e.g., block proportion, size distribution, block shapes, and block-matrix interfaces, significantly influence the mechanical and fracturing behaviours of these typical geomaterials. The uncertainty regarding the mechanical properties caused by these factors also creates great challenges for both engineering design and safety assessment (Raymond et al., 1984 and 2002; Medley 1994 and 2002).

Numerous laboratory investigations have been conducted in recent decades to understand the failure patterns and dominant influencing factors of these complicated geomaterials (Wang et al., 2018; Sonmez et al., 2004; Sharafisafa et al., 2020). Previous studies have shown that the mechanical properties are strongly related to the inclusion features, among which the block proportion (BP) is believed to be a dominant factor affecting the mechanical behaviours (Napoli et al., 2018; Lindquist et al., 1994; and Kalender et al., 2014). The mechanical strength, elastic modulus, and friction angles tend to increase with increasing BP (ranging from 20%~65%), as the block inclusions contribute strong mechanical properties. Other influencing factors, such as the block shape and size distribution, affect the interactions between blocks and the matrix (Sonmez et al., 2016 and Li et al., 2013). The failure characteristics are also significantly influenced by the interface strength. According to previous studies, the fracture paths will negotiate tortuously around contained blocks and develop irregularly throughout the matrix in most cases (Li et al., 2013 and Zhu et al., 2020). However, experimental results show that fractures can also pass through block inclusions when contained blocks are relatively weak or the matrix is well bonded (Wang et al., 2018 and Sonmez et al., 2006). For instance, in the uniaxial compression tests conducted by Sonmez et al., (2004 and 2006), the cracking paths of volcanic agglomerates were able to break through rock blocks. Sharafisafa et al., (2020) also found that tensile cracks can go through block inclusions when they lie perpendicular to the loading direction in Brazilian tests. Additionally, Medley et al., (2011) found that a high confining pressure will lead to block cracking, especially in the case of a high BP. Overall, the fracturing behaviours of the matrix and block inclusions impose notable effects on the mechanical responses of heterogeneous geomaterials. Thus, developing an effective method that can fully consider the microstructures and failure patterns of contained blocks is vital.

Since it is difficult to observe the micromechanical behaviours and internal interactions between the matrix and blocks through traditional experimental apparatuses, numerical methods would be helpful for investigating both the macro- and microcharacteristics of heterogeneous geomaterials.

Many simulations have been carried out to consider their randomised microstructures. For instance, researchers used regular geometries, such as spheres, ellipsoids, and polyhedrons, to represent block inclusions (Emad et al., 2019; Coli et al., 2012; Xu et al., 2015), which might be applicable to quantify the effect of the BP on the mechanical properties. However, realistic shape effects cannot be accurately captured using regular block geometries. With the advancement of block reconstruction techniques, more realistic block shapes can be obtained. For example, the two-dimensional (2D) profiles and three-dimensional (3D) morphologies of natural rock blocks can be reconstructed through digital image processing (DIP) and 3D scanning methods, respectively (Joseph et al., 2013 and Liang et al., 2019). On this basis, some researchers have investigated the block shape effects on the shear strength and failure behaviours (Zhu et al., 2020 and Gong et al., 2019). However, the shape features of blocks cannot be freely manipulated through this approach. To quantitatively control the shape features of block inclusions, other researchers have introduced spherical harmonic (SH) functions to digitalize the morphology of contained blocks (Wang et al., 2019 and Zhou et al., 2015). Then, a numerical model of composite materials containing massive stochastic and irregular blocks can be generated in a rapid and precise manner (Nie et al., 2020). Nevertheless, the interfaces among the blocks and matrix could not be precisely captured and replicated. In addition, Xu et al., (2016) and Lai et al., (2019) built a framework to reconstruct realistic particle morphologies based on the discrete pixel information of CT images. However, the scale of the particles reconstructed through the CT method is quite limited. A desirable block morphology is difficult to obtain when the components are rather densely packed. Furthermore, none of the abovementioned studies have fully considered the fracture behaviours of rock blocks.

Most recently, simulations combined with an advanced block reconstruction method have been developed as a powerful tool to understand the mechanical behaviours of heterogeneous geomaterials, among which the discrete element method (DEM) is one of the most promising techniques. However, different from experimental observations, most previous DEM research treated rock blocks as unbreakable assemblies during the loading process (Liang et al., 2019; Zhu et al., 2020 and Gong et al., 2019). In fact, the cracking and failure behaviours of block inclusions also play an irreplaceable role in determining the mechanical properties of geomaterials, especially when the rock blocks are relatively weak (Wang et al., 2018; Xu et al., 2008; Sonmez et al., 2004 and Sharafisafa et al., 2020). Additionally, block-containing materials cannot be treated as either a complete set of discrete media or homogeneous continuous materials due to their physical nature. Therefore, it should be more appropriate to capture their mechanical responses through a hybrid approach with a combination of continuity and discontinuity.

The combined finite-discrete element method (FDEM) was first introduced at the end of the 1980s by Munjiza et al. (1995 and 2004) and was initially designed to model the fracture and fragmentation of cementitious materials (Morris JP et al., 2006). An open source Y-FDEM software package was developed by Munjiza, which included both 2D and 3D FDEM (Munjiza et al., 2004). The Y-FDEM was further developed into various separate FDEM software platforms, such as VGeST, Solidity and Y-geo (Farsi A et al., 2021; Mahabadi O et al., 2012). These functional platforms significantly improved the applicability of the FDEM. In addition, several developments in FDEM codes were also accomplished by the Chinese Academy of Science (Sun L et al., 2020). Yan's studies make simulating fracture problems caused by multiphysics possible with FDEM (Yan.et al., 2019, 2021). Although FDEM models have been extensively applied in the scientific literature, a limited number of examples are able to efficiently model the mechanical and fracturing responses of heterogeneous geomaterials with irregular inclusions, which needs to consider shape effects and block breakages.

To overcome the abovementioned limitations in existing works, this study aims to develop a 3D hybrid approach to simulate heterogeneous geomaterials with block inclusions considering 3D irregular block shapes, the block-matrix interface, and block inclusion breakage. First, a deep convolutional neural network and computational geometry algorithms are employed to automatically reconstruct a shape library of rock blocks from raw images. Subsequently, a morphing technique is utilised to reconstruct the 3D rock block surface from selected 2D profiles with the desired block shapes. Next, based on a unique overlapping detection algorithm, blocks with specified proportions and gradations are randomly allocated to the sample domain to reproduce the realistic geometry model. The finite-discrete element model is further developed by integrating cohesive elements into the mesh in a fast and efficient manner, and the cohesive zone model is adopted to consider the failure behaviours of both the rock and the block-matrix interface. Afterwards, a series of physical and numerical Brazilian split tests are conducted on synthetic specimens to validate the reliability of the proposed approach from 2D to 3D. Finally, the effects of the block properties and interface strength on the mechanical properties are further investigated using the calibrated model.

2 Methodologies

2.1 Database establishment of 2D block inclusion outlines

Based on the authors' previous implementations (Liang et al., 2019), the well-acknowledged fully convolutional neural network (FCN), known as the U-NET, is employed to automatically extract

the block profiles from the raw images of the heterogeneous rock specimen. The raw image, binary mask and final output results of the identified rock block masks from the U-NET deep neural network are illustrated in Fig. 1.

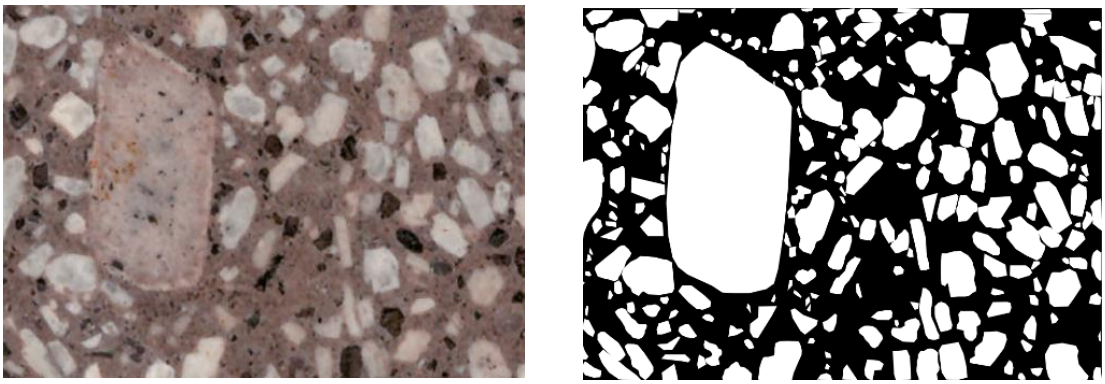

(*a*) raw image (*b*) binary mask

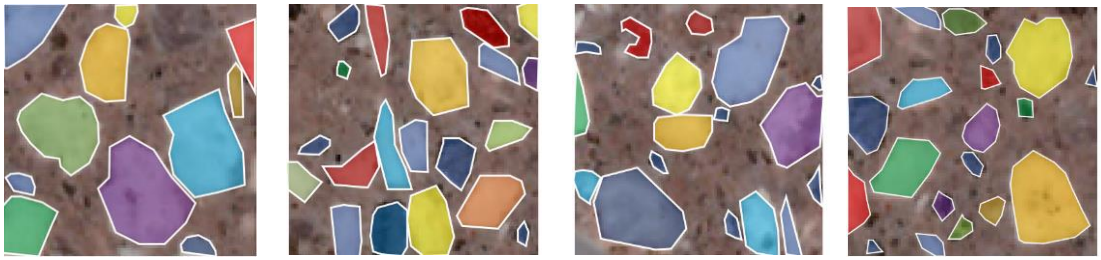

(*c*) final output of identified rock blocks

Fig. 1 Block profile extraction process

Generally, the images obtained through the trained network still have some defects, which affects further morphological analysis and calculation. To solve the problem induced by holes, a relatively mature pore filling algorithm can be used. For the segmentation of connected blocks, the classic corrosion-flooding method is employed to separate the connected blocks. The specific process is illustrated in Fig. 2 (a). Some of the individual rock block results that are identified and segmented from a raw image of heterogeneous rocks are shown in Fig. 2 (b).

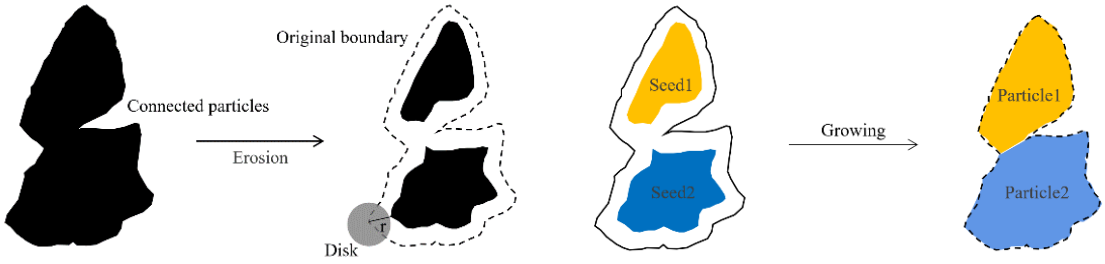

(a) Corrosion-flooding process

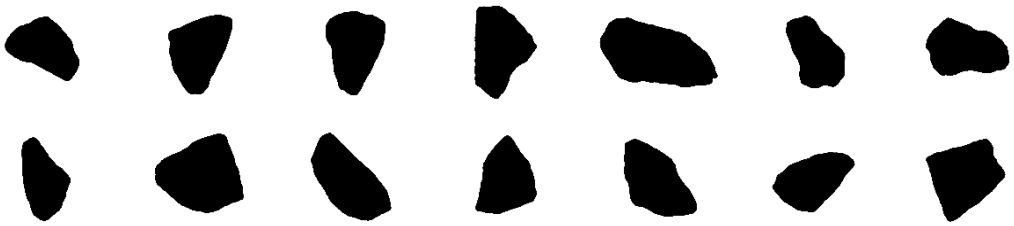

(b) Some examples of the rock blocks

Fig. 2 Obtaining 2D profiles of realistic rock blocks

After acquiring realistic outlines of the blocks, the next step is to calculate the shapes at various scale levels, as acknowledged in many previous studies (Nie et al., 2018 and Wang et al., 2019). The shape descriptors (as shown in Fig. 3) at different scale levels are briefly summarised as follows:

(1) Evaluation of the aspect ratio

To reflect the block contour, the aspect ratio (AR) is often used, as follows:

$$AR = D_{minor} / D_{major} \tag{1}$$

where D_{minor} is the width along the minor principal axis and D_{major} is the length along the major principal axis. Note that D_{minor} is also the measurement of the block sizes. Obviously, a smaller AR value represents a greater slenderness of the block.

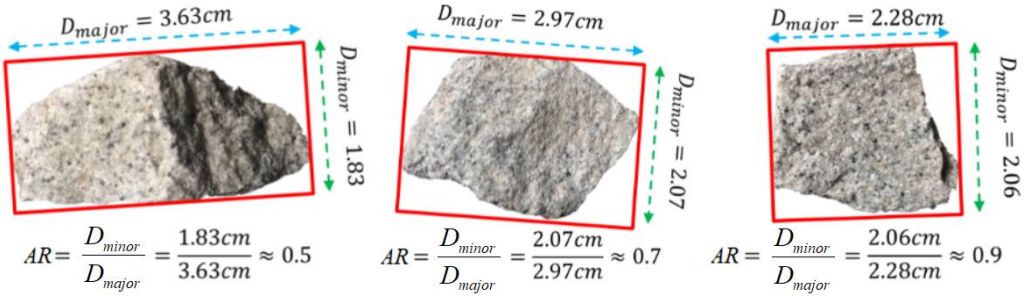

(a) aspect ratios

(b) roundness

Fig. 3 Examples of the block shape calculation procedure

(2) Evaluation of the block roundness

Roundness (Rd) reflects the sharpness and smoothness of the block corners; it can be calculated by the ratio between the mean curvature of the block corner and the radius of the maximum inscribed circle of the block contour, as follows:

$$Rd = \frac{\sum_{i=1}^{n_c} r_i}{n_c R_{insc}} \quad (2)$$

where r_i is the radius of the i_{th} corner circle of the block (in red), n_c is the number of corner circles, and R_{insc} is the radius of the maximum inscribed circle (in yellow). The algorithm to compute Rd is detailed in the author's previous study (Nie et al., 2018).

(3) Establishment of the rock block database

To facilitate retrieval and sample preparation, the shape indicators of the rock blocks are stored together with the coordinates, storage format number, outline, aspect ratio and roundness. Notably, all the 2D outlines are installed based on the following criteria:

(a) For each outline, the geometric centre is taken as the origin, and the block is rotated to ensure that the major orientation is parallel to the positive direction of the *x*-axis;

(b) The block size is normalised so that the longest axial length of the block is equal to 1;

(c) The discrete points are resampled from the 2D outline based on the cubic interpolation method.

The selection of rock blocks from the block library is performed as follows:

(a) The ranges of the desired shape parameters are input.

(b) According to the range of these values, the 2D contour that meets the requirements can be searched automatically.

(c) The visualised two-dimensional contour is selected and output.

After establishing the block library, selecting the 2D contours of the blocks that meet specific requirements to facilitate the realistic reconstruction of 3D blocks is very convenient.

2.2 Stochastic reconstruction of a 3D heterogeneous specimen

The 2D block outlines with specified shapes are randomly selected from the established block library to regenerate the geometry model of the 3D blocks. The employed algorithms have been proposed and validated in previous studies (Mollon et al., 2013). The procedure is detailed as follows:

(1) First, based on the 3D block shapes EI_{3D} and FI_{3D} (the definition can be found in the literature (Su et al., 2020 and Nie et al., 2018)), determine the AR_a, AR_b, and AR_c of the three 2D block outlines, a, b, and c, respectively, as follows:

$$AR_a = EI_{3D} \cdot FI_{3D}\ ,\ AR_b = EI_{3D}\ ,\ AR_c = FI_{3D} \quad (3)$$

It should be noted that the selected outlines a, b, and c are expected to match the top view projection (xoy plane), front view projection (xoz plane) and side view projection (yoz plane) of the reconstructed 3D block, respectively, as shown in Fig. 4(a~c).

(2) Then, based on the determined AR_a, AR_b, and AR_c, three 2D outlines are selected from the established block database that have aspect ratios similar to the desired ones. To minimise the differences between the aspect ratios of the selected outlines AR'_a, AR'_b, and AR'_c with the desired values, a threshold value δ is defined for the selection of the 2D outlines, as follows:

$$\delta = \frac{1}{3}\left(\frac{\left|AR_a - AR_a^{'}\right|}{AR_a} + \frac{\left|AR_b - AR_b^{'}\right|}{AR_b} + \frac{\left|AR_c - AR_c^{'}\right|}{AR_c} \right) \tag{4}$$

where the allowance is reserved to facilitate retrieval of 2D outlines.

(3) Next, since the aspect ratios of the selected 2D outlines may be different from the desired values, AR_a, AR_b, and AR_c, it is necessary to adjust the shapes of the selected 2D outlines to ensure that the selected 2D outlines can match each other at the intersection points in 3D space, as shown in Fig. 4(d). The following methodology is employed to ensure that the intersection points coincide with each other. Taking the x-axis as an example, if $x_b^1 \neq x_c^1$ and $x_b^2 \neq x_c^2$, then outline b remains unchanged, and outline c can be stretched by the following:

$$x_c^i = \left(x_c^i - x_c^1\right)\frac{\left(x_b^2 - x_b^1\right)}{\left(x_c^2 - x_c^1\right)} + x_b^1 \tag{5}$$

With the same adjustment being applied in the y-axis and z-axis, the intersection points will share the same coordinates.

(4) The outline points (x, y) are transformed from Cartesian coordinates into polar coordinates. Then, the three selected 2D outlines a, b, and c are positioned into the 3D spherical coordinate system to form a curve skeleton, as shown in Fig. 4-d. In the next step, a continuous block surface $R(\theta, \varphi)$ is generated from the curve skeleton. Note that the generated $R(\theta, \varphi)$ should match the outlines in all three view projections.

(5) 3D interpolation algorithms (Mollon et al, 2013) are employed in this study. Taking the first quadrant as an example ($\theta \in [0, \pi/2]$), the generation process of the block surface is as follows:

Step 1: For half curve b_1 where $\theta = 0$, a revolutionary solid surface $R_{b_1}(\theta, \varphi)$ is generated by rotating b_1 around the z-axis, as follows:

$$R_{b1}(\theta,\varphi)=\begin{cases} r_b\left(\frac{1}{2}\pi-\varphi\right) & \varphi\in\left[0,\frac{1}{2}\pi\right],\theta\in\left[0,\frac{1}{2}\pi\right] \\ r_b\left(\frac{5}{2}\pi-\varphi\right) & \varphi\in\left[\frac{1}{2}\pi,\pi\right],\theta\in\left[0,\frac{1}{2}\pi\right] \end{cases} \tag{6}$$

Step 2: R_{b_1} is stretched horizontally to ensure that the section outline of the newly generated surface R'_{b_1} matches the 2D outline a in the xoy plane, as follows:

$$R'_{b1}(\theta,\varphi)=R_{b1}(\theta,\varphi)\left[1+\left(1-\frac{|\varphi-\pi/2|}{\pi/2}\right)\cdot\frac{r_a(\theta)-r_a(0)}{r_a(\theta)}\right] \tag{7}$$

Step 3: To obtain a smooth block surface, $R'_{b1}(\theta,\varphi)$, where $\theta=\pi/2$, should match the half curve c_1. Thus, the surface R'_{b_1} should be further revised by the following:

$$R(\theta,\varphi)=R'_{b_1}(\theta,\varphi)+\frac{\theta}{\pi/2}\left[R'_{c_1}(\theta,\varphi)-R'_{b_1}(\theta,\varphi)\right]\quad \varphi\in[0,\pi],\theta\in[0,\pi/2] \tag{8}$$

By repeating the same procedure in the remaining quadrants, a smooth 3D block surface is obtained. Examples of the 3D block inclusions reconstructed from the 2D outlines are shown in Fig. 44(e). Compared with the original cross-section, each shape of the original block inclusion is preserved.

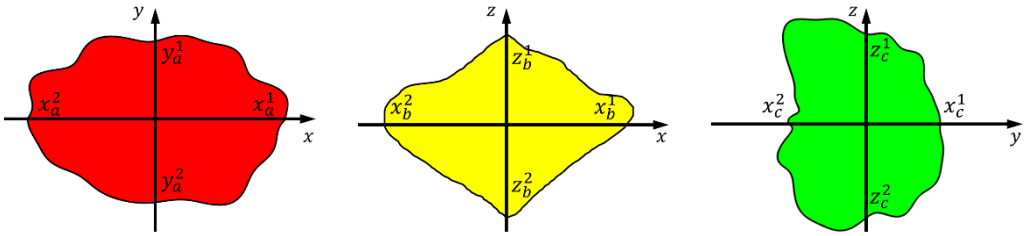

(*a*) Outline a (*b*) Outline b (*c*) Outline c

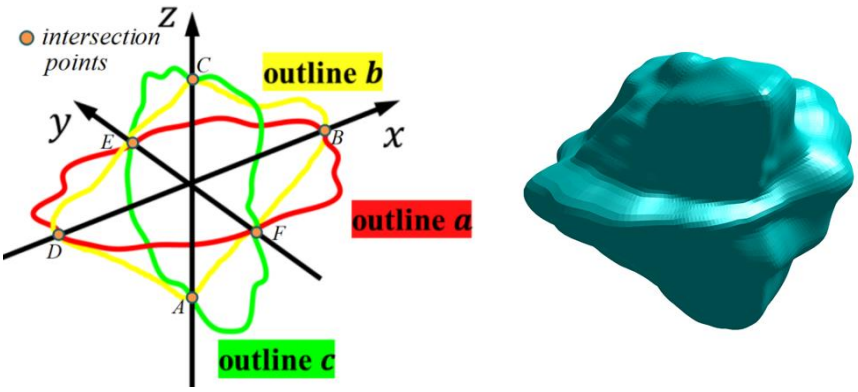

(*d*) Their position in 3D space (*e*) The reconstructed 3D block surface

Fig. 4 Examples of the 3D block inclusions reconstructed from the 2D outlines

After the 3D block inclusions are reproduced, the next step is to randomly allocate the generated

block inclusions into the predefined specimen domain. In addition to block shapes, two main rock block features, i.e., the block proportion and gradation, are quantitatively controlled based on the following algorithms:

(1) Rock block proportion

Assuming the desired total volume of the sample domain is V_{Total} and the block proportion is W_{block}, the volume of the solid blocks can be determined by the following:

$$V_{Block} = V_{Total} \times W_{block} \tag{9}$$

(2) Rock block gradation

Assuming that $P(r_i)$ is the cumulative volumetric percentage of blocks with size r (equivalent radius) being smaller than r_i, $P(r_i)$ follows fractal theory, as follows (Xu et al., 2018):

$$P(r_i) = \frac{V(r \le r_i)}{V_{Block}} \approx \left(\frac{r_i}{r_{max}}\right)^{3-D} \tag{10}$$

Assuming the number of block inclusions to be allocated is N_{Total} and the number of blocks with size r smaller than r_i is $N(r_i)$, as follows:

$$N(r_i) = \int_{r_{min}}^{r_i} dN(r_i) \tag{11}$$

where $dN(r_i)$ can be derived from $dV(r_i)$, as follows:

$$dN(r_i) = \frac{dV(r_i)}{\frac{4}{3}\pi {r_i}^3} = \frac{V_{Block} dP(r_i)}{\frac{4}{3}\pi {r_i}^3} \tag{12}$$

Next, based on the above equations, we can obtain the following:

$$N(r_i) = \int_{r_{min}}^{r_i} dN(r) = \frac{3V_{Block}(3-D)}{4\pi D {r_{max}}^{3-D}} ({r_{min}}^{-D} - {r_i}^{-D}) \tag{13}$$

Thus, once D, r_{min}, and r_{max} are given, N_{total} can be obtained by the following:

$$N_{total} = N(r_{max}) = \frac{3V_{Block}(3-D)}{4\pi D {r_{max}}^{3-D}} ({r_{min}}^{-D} - {r_{max}}^{-D}) \tag{14}$$

Then, the integer number i is substituted from N_{total} to 1 to obtain the size r_i of the i_{th} block, as follows:

$$r_i = \left[{r_{min}}^{-D} - i\frac{4\pi D {r_{max}}^{3-D}}{3V_{Block}(3-D)}\right]^{D} \tag{15}$$

Finally, the desired volume of the block can be determined as follows:

$$V_i = \frac{4}{3}\pi \left[{r_{min}}^{-D} - i\frac{4\pi D {r_{max}}^{3-D}}{3V_{Block}(3-D)}\right]^{3D} \tag{16}$$

(3) Rock block shapes and orientations

The scheme to control the elongation and flatness of the generated 3D block is mentioned in the

previous section. EI_{3D} and FI_{3D} can be predefined through the selection of the appropriate 2D outlines a, b, and c with $AR_a = EI_{3D} \cdot FI_{3D}$, $AR_b = EI_{3D}$ and $AR_c = FI_{3D}$. Once the 3D block surface $R_i(\theta, \varphi)$ is reconstructed from the 2D outlines, we can compute the specific volume v_i as follows:

$$v_i = \int_0^{2\pi} \int_0^{\pi} \frac{R_i(\theta,\varphi)^3}{3} d\varphi \, d\theta \tag{17}$$

Then, the size factor k_i can be obtained to scale the surface points so that the allocated block has an identical volume to the desired block, as follows:

$$k_i = \sqrt[3]{V_i / v_i} \tag{18}$$

Based on k_i, the scaled ${R_i}^{gen}(\theta, \varphi)$ of the generated block inclusions can be obtained as follows:

$${R_i}^{gen}(\theta, \varphi) = k_i R_i(\theta, \varphi) \tag{19}$$

For the orientation, the initial model of the generated block inclusion is expected to have the major principal axis parallel to the x-axis. Thus, if the orientation $\left(\theta_i^{rot}, \varphi_i^{rot}\right)$ of the i_{th} rock block is specified, then ${R_i}^{gen}(\theta, \varphi)$ can be further computed by the following:

$${R_i}^{gen}(\theta, \varphi) = k_i R_i\left(\theta + \theta_i^{rot}, \varphi + \varphi_i^{rot}\right) \tag{20}$$

After the virtual rock blocks with the specific shapes and desired sizes are determined, the final step is to reconstruct the stochastic model of geomaterials with randomly distributed block inclusions. Note that to ensure nonoverlap among block inclusions, the following procedure is performed to randomly allocate the block inclusions into the sample domain from the largest to the smallest:

(1) The desired sample domain is defined as a cylinder with a diameter of L and a thickness of H, and the origin of the global coordinate system is at the centre of the box.

(2) For each block inclusion to be allocated, the x_{max}, x_{min}, y_{max}, y_{min}, z_{max}, and z_{min} of the surface points are computed using their local coordinate system, which can be easily obtained by transforming spherical coordinates into Cartesian coordinates. Then, the location of the rock block centre (x_c, y_c, z_c) using the global coordinate system can be randomly determined based on the following equations:

$$\begin{aligned} x_c &= \varepsilon_r \cdot L \cdot cos\left(\varepsilon_\theta \cdot 2\pi\right)/2 \\ y_c &= \varepsilon_r \cdot L \cdot sin\left(\varepsilon_\theta \cdot 2\pi\right)/2 \\ Z_c &= \varepsilon_z \cdot H \end{aligned} \tag{21}$$

where ε_r, ε_θ, and ε_z are random numbers ranging from 0 to 1.

(3) Then, the overlapping condition among the allocated blocks is checked with the existing ones. Assume that blocks A and B are the pair of allocated and existing blocks. The following substeps are conducted:

Step 1: The axis-aligned bounding box of each block is determined by (P_{min}, P_{max}), as follows:

$$P_{min} = \left[x_{min} - x_c \quad y_{min} - y_c \quad z_{min} - z_c\right]$$
$$P_{max} = \left[x_{max} + x_c \quad y_{max} + y_c \quad z_{max} + z_c\right] \tag{22}$$

Step 2: The overlapping detection algorithm (Sulaiman et al, 2014) is employed to check the overlapping condition between bounding boxes $\left(P_{min}^A, P_{max}^A\right)$ and $\left(P_{min}^B, P_{max}^B\right)$. If the bounding boxes do not overlap, then blocks A and B do not overlap. If the bounding boxes overlap, then Step 3 must be conducted.

Step 3: Block A is discretized into N_p points, while block B is represented by the continuous surface function $R^B(\theta, \varphi)$ with their local spherical coordinate system. For each surface point ${R_i}^A(\theta_i, \varphi_i)$, ${R_i}^A(\theta_i, \varphi_i)$ is transformed into the local spherical coordinate system of block B to obtain ${R_i}^{A\to B}\left({\theta_i}^{A\to B}, {\varphi_i}^{A\to B}\right)$. The penetration indicator Γ_i is computed as follows:

$$\Gamma_i = {R_i}^{A\to B}\left({\theta_i}^{A\to B}, {\varphi_i}^{A\to B}\right) - R^B\left({\theta_i}^{A\to B}, {\varphi_i}^{A\to B}\right) \tag{23}$$

If $\Gamma_i > 0$, then point ${R_i}^A(\theta_i, \varphi_i)$ does not overlap with block B, while if $\Gamma_i < 0$, then point ${R_i}^A(\theta_i, \varphi_i)$ intrudes into block B. If all surface points on block A are identified to be under the nonpenetration condition, then the allocated block A does not overlap with block B. The overall overlap detection process among blocks is illustrated in Fig 5 to provide better understanding.

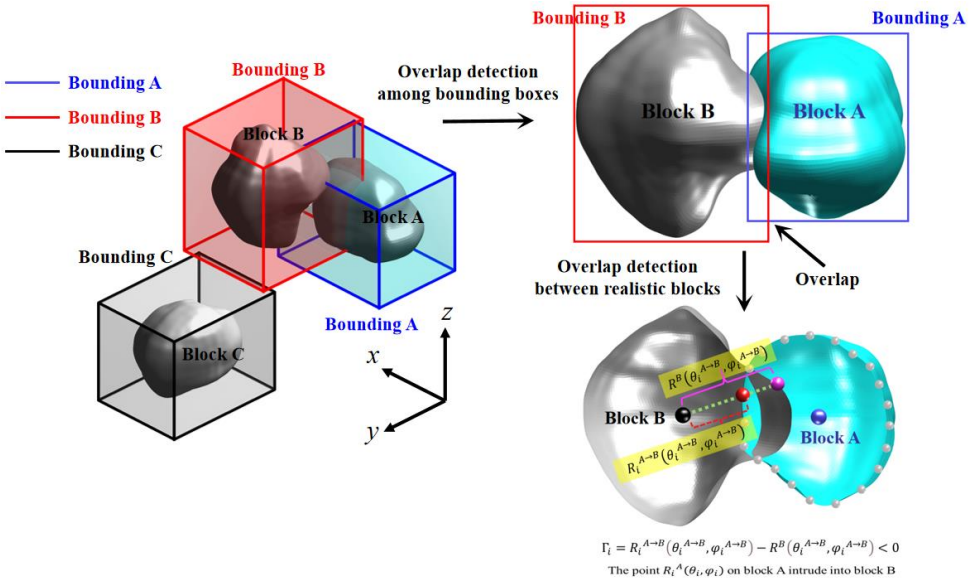

Fig. 2 Overall overlap detection among blocks

(4) Repeat step 3 until the allocated blocks do not overlap with all of the adjacent blocks.

(5) Repeat steps 2 to 4 until all the blocks are allocated.

Based on the above-detailed procedures, we can generate a stochastic model of realistic geomaterial models with desirable block inclusion features. Examples of the generated models with various BPs are illustrated in Fig. 6.

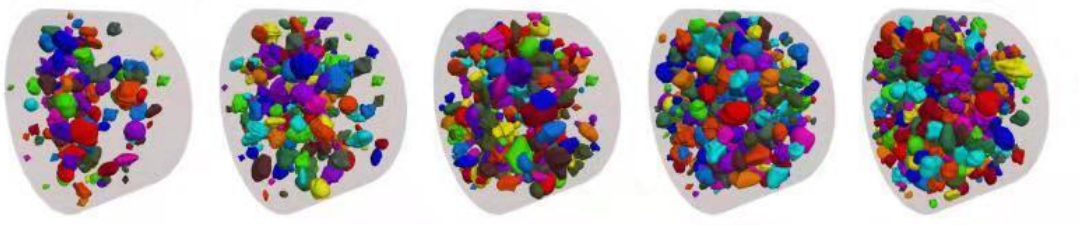

(a) 10% (b) 20% (c) 30% (d) 40% (e)50%

Fig. 6 Examples of the generated models with various BPs

2.3 Finite-discrete element model

The cohesive zone model was initially proposed by Barenblatt et al. (1959) and Dugdale et al. (1960). This model is designed to handle mechanical singularities in crack tips and to monitor mechanical behaviours such as material bonding, aggregate interlock, and surface friction (Yang et al, 2009). As discussed by Nguyen (2014), the cohesive element model is compatible with existing finite element codes and can effectively avoid the tremendous time cost of tedious contact searching, judging, and updating; thus, it is a good alternative choice for modelling the fracturing and failure behaviours compared to other methods (e.g., extended finite element method). The details of the 3D cohesive zone model can be found in the Appendix.

As fracture paths can be rather stochastic and irregular, cohesive elements are inserted ubiquitously into the finite meshes. The basic scheme is to replicate and renumber the nodes of the interfaces of adjacent elements and retain the coordinates of updated nodes. Thus, fabricated cohesive elements have a zero out-of-plane thickness. Taking the COH3D8 type of cohesive element as an example (as shown in the left of Fig. 6-a), the coordinates of points 1, 2, 3, and 4 on element A coincide with those of copied points 5, 6, 7, and 8 on element B, so the cohesive element (as shown in the right of Fig. 6-a) is formed with point sequences from 1 to 8. Notably, a consistent nodal ordering approach (anti-clockwise) of cohesive elements should be used to determine the correct normal direction of surface cracks.

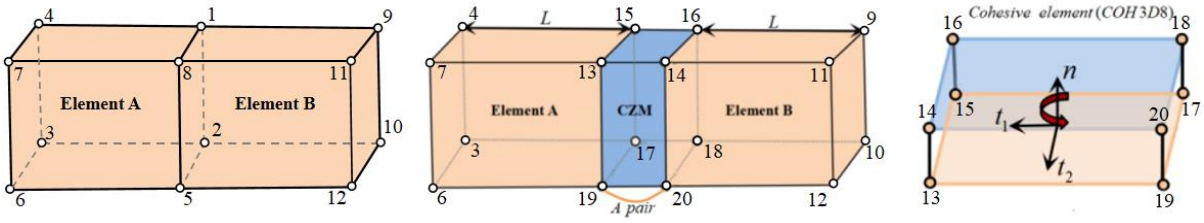

(a) Cohesive elements consisting of eight nodes

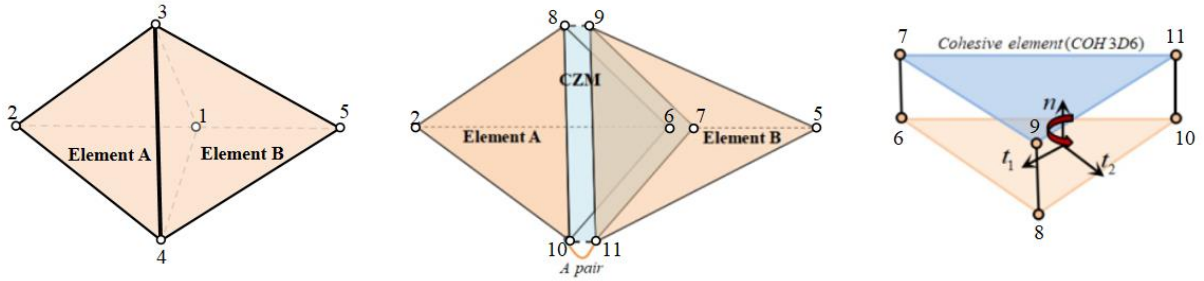

(b) Cohesive elements consisting of six nodes

Fig. 7 Structural characteristics of different cohesive elements

As the block surface is irregular, the nodal and elemental connectivity of the 3D numerical model is extremely complicated. An efficient algorithm is needed to robustly process the tremendous changes in the nodal and elemental information caused by the insertion of cohesive elements, which is accomplished by the following steps:

(a) The nodal and elemental data of all solid elements are read from a meshed model. Fundamental information includes the nodal coordinates, nodal labels, nodal connectivity, and elemental labels. Then, both the nodal and elemental databases are generated to store the corresponding information.

(b) The element faces can be categorised into two groups, i.e., element faces between adjacent elements (shared faces) and faces on the geometric boundary (boundary faces). Note that only shared faces should be replaced by cohesive elements, as shown in Fig 7. For each node on the shared faces, the number of connected elements is calculated, which determines the replicating times of the node. Taking node 1 in Fig. 7 (a) for instance, both solid elements A and B are related to node 1. Thus, two new element nodes are generated to replace node 1.

(c) The coordinates of new nodes are consistent with those of the original nodes, whereas the labels of the new nodes are numbered from the maximum label of the original meshes. With the new nodes being labelled, the node connectivity of the connected solid elements is also updated.

Taking solid element A in Fig. 7(b) for instance, the node connectivity changes from 1-2-3-4 to 6-2-8-10 after node updating. Then, the changes in the nodal and elemental information are recorded in the aforementioned nodal and elemental databases.

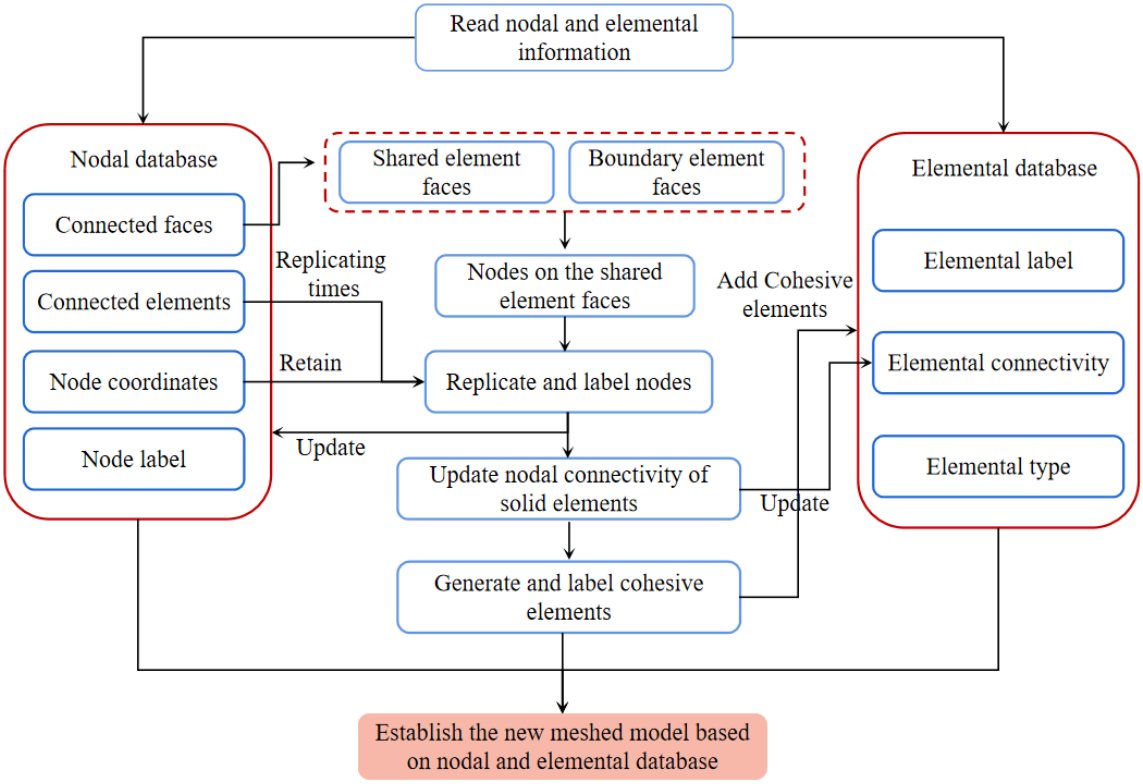

Fig. 8 Flowchart of the process of inserting cohesive elements ubiquitously

(d) For each inner face, three or four pairs of nodes can be found, which comprise a cohesive element (COH3D6 or COH3D8, as shown in Fig. 7). The cohesive elements are labelled from the last element label of the original meshed model. Then, the cohesive elements are classified into three groups, i.e., the rock, matrix and interface cohesive elements, based on the properties of two adjacent elements.

(e) Thereafter, the nodal and elemental information of both the updated solid elements and cohesive elements are well prepared. Finally, a new hybrid numerical model with inserted cohesive elements is accomplished.

The above procedure is clarified by the flowchart illustrated in Fig. 8.

3 Experimental validation

To carefully validate the proposed hybrid approach, the procedure employing only step 1 and step 3, as a simplified 2D approach, is first examined by preparing synthetic heterogeneous discs with

Brazilian split tests that are more homogeneous and easily controlled. Then, realistic 3D specimens are fabricated to examine the 3D approach with all three steps.

3.1 Validation of the approach simplified in 2D

3.1.1 Preparation of the experimental and numerical specimens

To validate the proposed hybrid numerical method, Brazilian split tests are performed on synthetic heterogeneous specimens for a comparison with the numerical results. Each disc has a diameter of 50 mm and a thickness of 25 mm. Inspired by existing studies (Sharafisafa et al., 2020), the matrix is composed of gypsum, while the rocks are made of Portland cement. The focus of this study is placed on precisely simulating the deformation behaviour and failure patterns of heterogeneous geomaterials using the developed hybrid numerical method. The purpose of choosing gypsum and Portland cement is to mimic two types of components with distinctive mechanical properties. To fabricate the synthetic specimens, geometric files are prepared first to generate the moulds of the specimens through 3D printing techniques, as shown in Fig 9(a). Note that block outlines are intentionally selected from the established block library. The procedure to manufacture artificial heterogeneous discs is detailed as follows.

(1) As shown in the first column of Fig. 9(a), three moulds with block proportions of 20%, 30%, and 40% are manufactured through 3D printing technology.

(2) The water gypsum ratio is set as 0.5. After mixing well, the gypsum liquid is poured into the moulds to generate the matrix component. After 20 seconds of vibration and 4 hours of curing, the matrix is demoulded.

(3) The water cement ratio is set as 0.4. Portland cement liquid is injected into the preset holes to generate the block components. Subsequently, these specimens are placed on a vibration platform for 20 seconds to remove any bubbles.

(4) Then, discs of pure gypsum and pure Portland cement are also generated to calibrate the mechanical properties of the hybrid numerical model. Finally, all the specimens were kept in a stable environment at a temperature of 20 °C for 7 days. The prepared specimens and experimental equipment are shown in Fig. 8 (b).

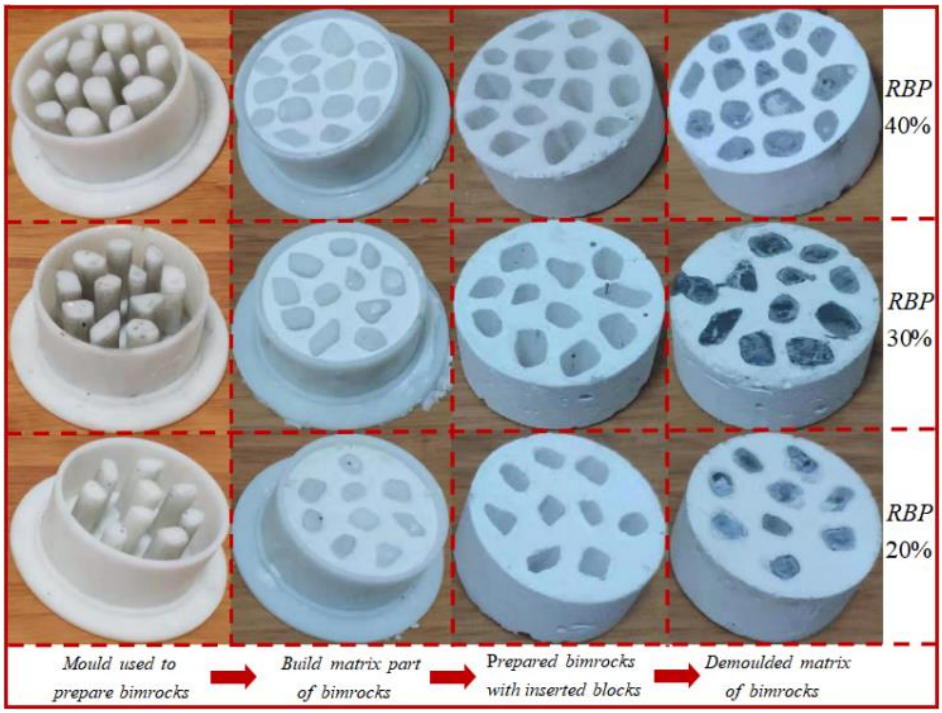

(a) The fabricating process of the synthetic specimens

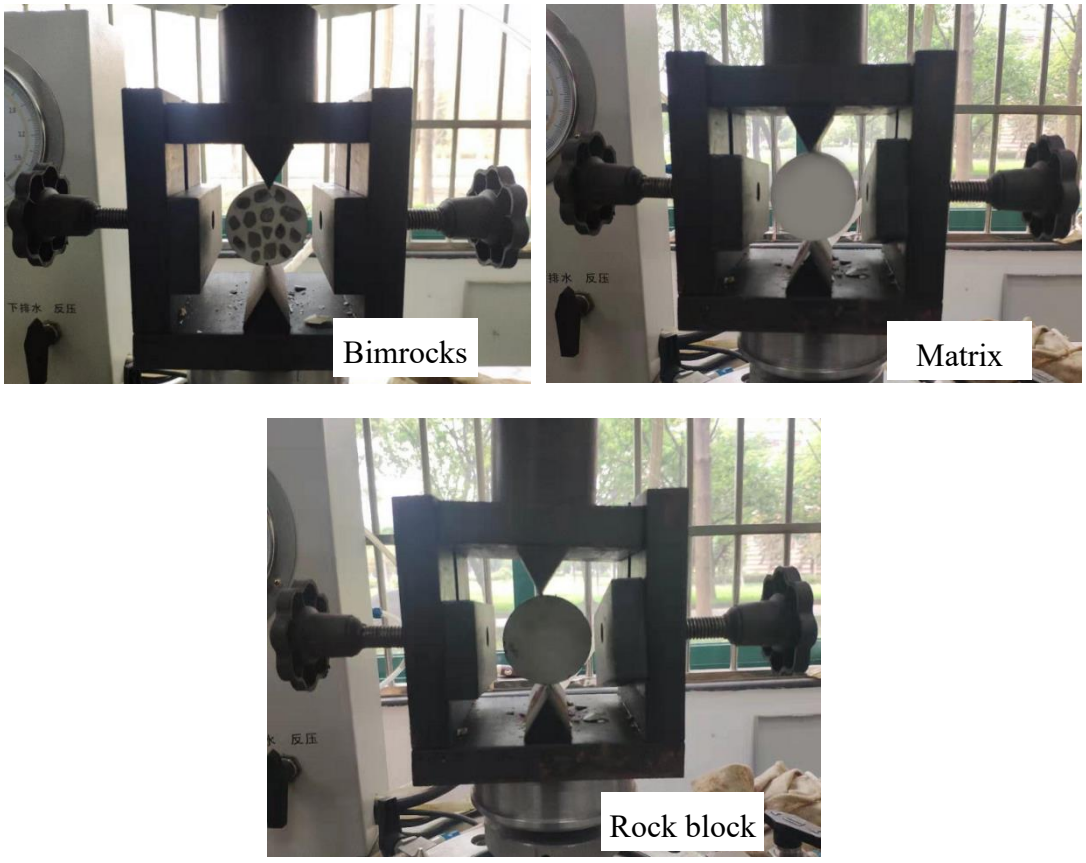

(b) The Brazil split test performed on different specimens

Fig. 9 Preparation of specimens and experimental apparatus

Brazilian tests are performed using a servo-controlled testing system with a maximum loading

capacity of 50 kN. The split tests are conducted with a loading speed of 0.2 mm/min. Simultaneously, hybrid numerical models are established using the same geometric files that were used to generate the moulds. Therefore, the synthetic specimens can be perfectly replicated in the numerical analysis since they share the same geometric files. Based on the matched geometry and same loading condition, virtual Brazil split tests are also conducted on the numerical models, as shown in Fig. 10. As mentioned in section 2.3, the cohesive elements embedded into all element interfaces are classified into three groups, as shown in Fig. 11.

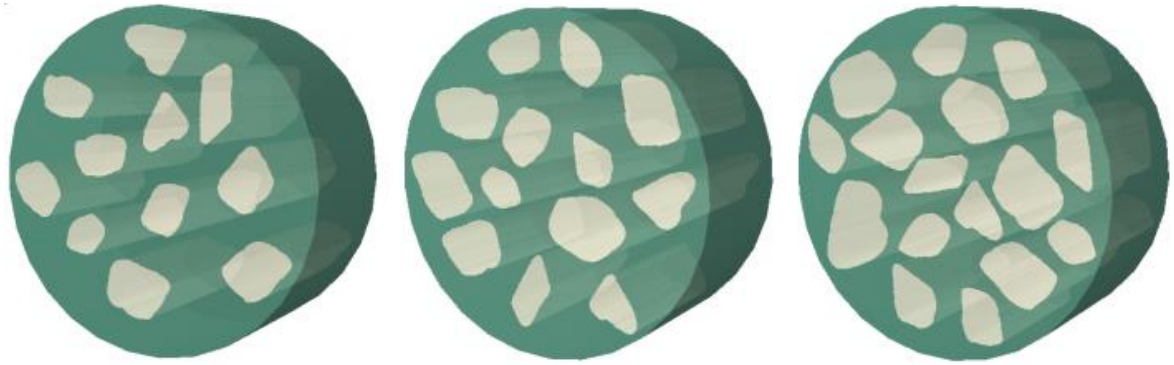

(a) Rock proportion 20% (b) Rock proportion 30% (c) Rock proportion 40%

Fig. 10 Numerical models of artificial heterogeneous specimens with various rock proportions

As shown in Fig. 9(b), additional tests are conducted on the pure gypsum and Poland cement specimens. Thus, the macroparameters, including the density, elastic modulus, Poisson's ratio, tensile strength and shear strength, can be directly obtained through the experimental results. However, the microparameters, i.e., stiffness, traction criteria and fracture energies, must be determined through a calibration process (Tatone et al., 2015). Thus, a series of trial and error tests are performed to adjust the microparameters. On the basis of previous research (Tatone et al., 2015 and Wu et al., 2018), the following basic rules are adopted in the calibration process:

(1) Large stiffness values of cohesive elements are suggested to ensure the correct elastic response. Among them, the shear stiffness is mostly weaker than the normal stiffness for geological materials (Jiang et al., 2018, Wei et al., 2019 and Zhou et al., 2020).

(2) The traction criterion and fracture energies in the shear directions may be larger than those in the normal directions according to conclusions from previous research on rock materials (Tatone et al., 2015, Wei et al., 2019 and Zhou et al., 2020)

(3) The Brazilian disc strength is assumed to be a function of fracture energy. First, the fracture energies are adjusted to find an appropriate parameter combination that yields both the correct strengths and realistic fracture patterns. While none of the combinations can achieve the target strength, the traction criteria of the interfaces are then changed. Subsequently, another iteration process of fracture energies is carried out again.

After the carefully designed calibration process, the macro-micro mechanical parameters of the

proposed numerical model are illustrated in Table. 1. Note that the modelling approach can also be combined with optimisation methods or the transitional Markov chain Monte Carlo method to efficiently identify all the mechanical parameters (Yin et al., 2017, 2018; Jin et al., 2019, 2020).

Table 1 Mechanical parameters of the numerical model

Mechanical parameters	Rocks (Poland cement)	Matrix (gypsum)	Cohesive elements		
			Matrix	Interface	Rocks
Elastic modulus/MPa	20000	4000	--	--	--
Poisson's ratio	0.22	0.3	--	--	--
Tensile stiffness (GPa/m)	--	--	2000	1500	10000
Shear stiffness (GPa/m)	--	--	600	450	4000
Normal traction criterion/MPa	--	--	1	0.8	2
Shear traction criterion/MPa	--	--	1.5	1.2	3
Mode-I fracture energy (N/m)	--	--	50	40	100
Mode-II-fracture energy (N/m)	--	--	100	80	200

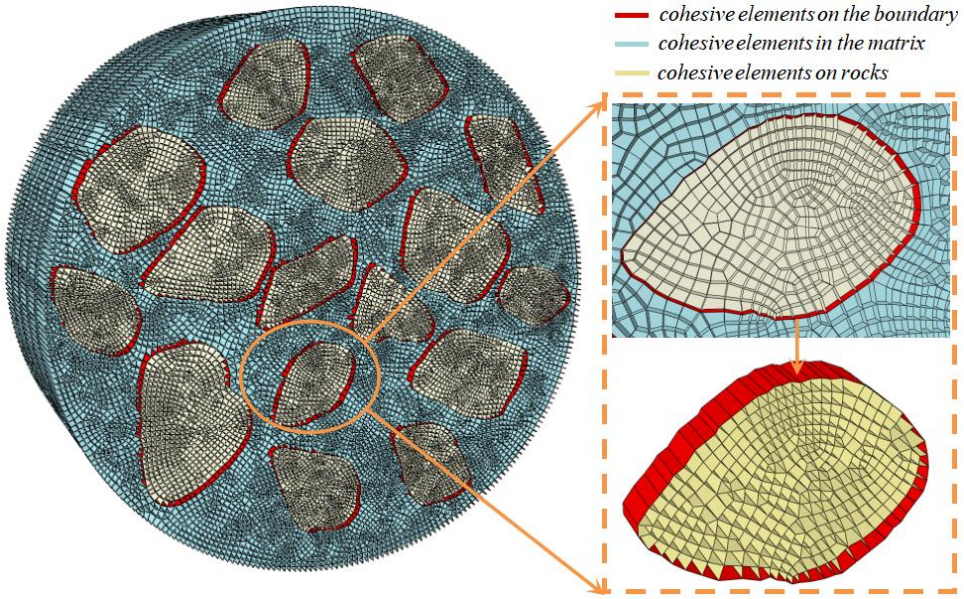

Fig. 31 Insight regarding the embedded cohesive elements

3.1.2 Results of the Brazilian tests and comparison

The failure characteristics of both the numerical modelling and experimental results are depicted in Fig. 12. As observed from the figure, the numerical results show failure patterns consistent with the experimental results. Due to the significant mechanical contrasts of the components and irregular geometry of block inclusions, stress concentrations can easily occur at the interfaces between the matrix and block inclusions. Thus, cracking is most likely to develop along the block-matrix

458 interfaces. For the specimen with a BP of 20%, the crack first initiates around the matrix-block
459 interfaces and then develops almost vertically through the matrix. The failure patterns are similar to
460 those of a homogeneous brittle material owing to the relatively low rock proportion. With increasing
461 rock proportion, the failure patterns become much more irregular and complicated, as shown in the
462 specimen with a BP of 30%. Tortuous fracture surfaces, the detachment of blocks at interfaces, and
463 localised failure are observed. As the BP reaches 40%, the block components seriously restrict crack
464 propagation. It should be noted that block breakage is found at the top of the specimens since the
465 block happens to lie vertically along the crack paths. It is inferred that the mechanical properties of
466 heterogeneous geomaterials can benefit from the increase in BPs. The increasing rock block would
467 further constrain the crack propagation and improve the overall strength due to their own mechanical
468 strength advantage. Therefore, it is necessary to consider the breakage of a block when the modelling
469 block contains geomaterials.

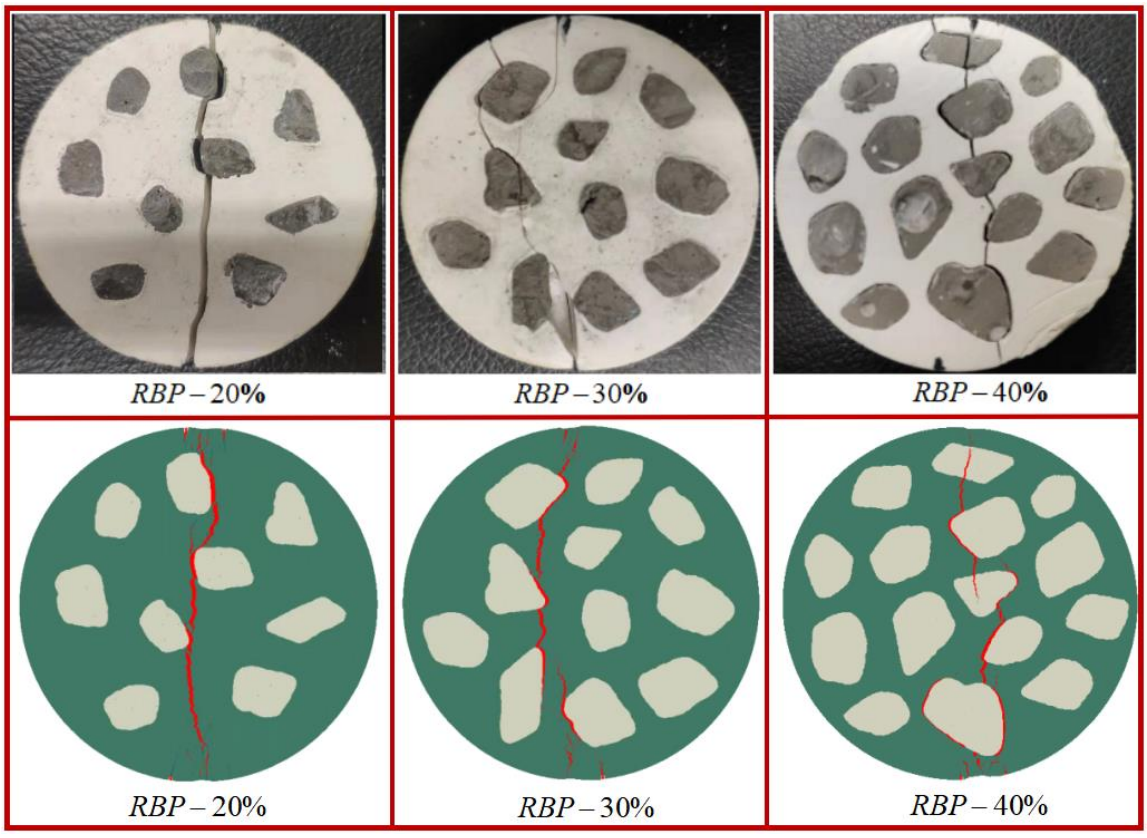

470

471 Fig. 42 Comparison of fracture characteristics from the numerical and experimental results

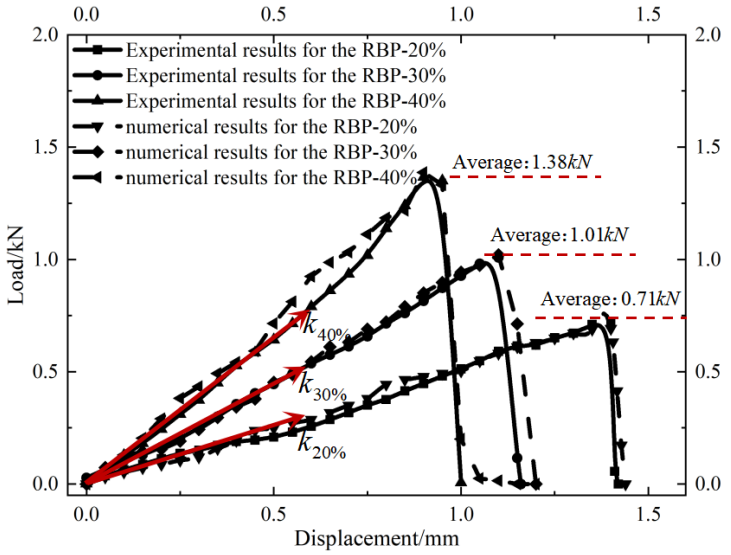

Fig. 53 Comparison of the load-displacement curves from the numerical and experimental results

The comparison of the load-displacement curves from the numerical and experimental results is illustrated in Fig. 13. The numerical results agree well with the experimental results. It is apparent that the split strength and elastic modulus of the specimens improve with increasing BPs. In the initial elastic phases, the numerical results show limited fluctuations caused by the strain concentrations and sudden detachment of the block-matrix boundary (Sharafisafa et al., 2020), which correspond with the conclusion found in previous research. For specimens with BPs of 20% and 30%, the load dropped dramatically after the peak strength. However, fluctuations and limited plastic deformation are found near the peak zone of specimens with BPs of 40%. Inspired by previous research (Sharafisafa et al., 2020), these fluctuations are caused by the abrupt breakage and interlock effects of rock blocks along the loading direction. Thus, the failure of rock blocks could impose noticeable effects on the behaviour of block-containing geomaterials.

3.2 Validation of the 3D approach with whole steps

3.2.1 Preparation of the experimental and numerical specimens

To further validate the proposed 3D approach with all three steps, synthetic specimens with block inclusions are fabricated and tested. The components of the synthetic specimens, as illustrated in Fig. 14, include crushed limestone stone and red clay. Inspired by the experiments in the existing publications (Afifipour et al., 2014; Wang et al., 2015 and Li et al., 2020), the matrix is fabricated by mixing red clay with moderate cement to resume the cemented state. Additionally, three specimens with 50 mm diameters and 25 mm thicknesses are cored from intact limestone to obtain the basic mechanical properties of rock blocks, and three specimens of pure cemented red clay are also prepared to calibrate the mechanical properties of the matrix. Four groups of test specimens, with desired rock proportions ranging from 20% to 50%, were prepared for validation. Nine specimens were prepared for each group, and the specific weights of each component for each group are illustrated in Table 2.

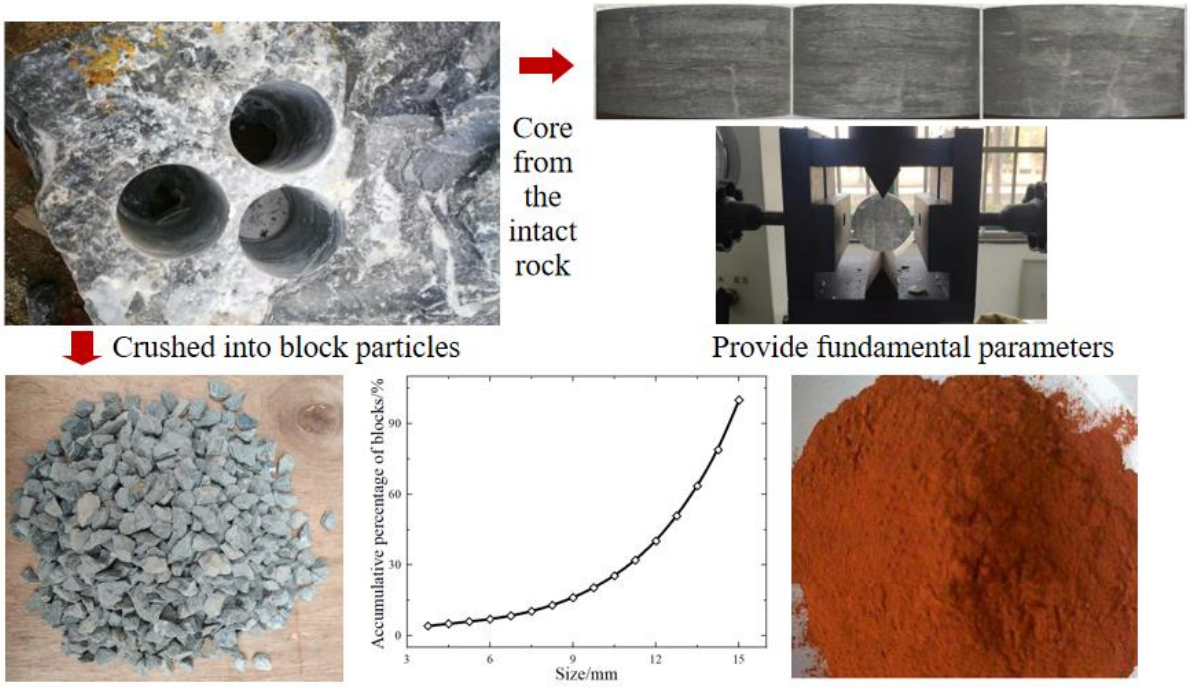

Fig. 14 Components of the fabricated specimens

Table 2 Weight of each component for every 10 kg of each validation group

Group No,	RBP %	Cement (C50) kg	Red clay kg	Water kg	Blocks kg
A	0	1.64	5.47	2.90	/
B	20	1.31	4.39	2.31	2.0
C	30	1.14	3.85	2.01	3.0
D	40	0.98	3.30	1.73	4.0
E	50	0.81	2.75	1.44	5.0

The major steps to fabricate the heterogeneous specimens include (1) adding the red clay, cement, rock blocks, and water into the mixing machine in sequence and stirring; (2) pouring the mixtures into the mould (as shown in Fig. 15 (a)) and compacting the mixture using a vibration table for 5 minutes; (3) keeping the specimens in the mould for 24 hours and then demoulding the specimens; (4) keeping the specimens in a moist environment at a temperature of approximately 25 °C and relative humidity of 95% for 7 days for curing; and finally (5) polishing both ends of the specimens (Fig. 15 (a)).

To generate a numerical model that mimics the realistic rock block shapes of the test specimens, some of the obtained cylinder test specimens are cut in the middle first to expose the inner sections (Fig. 15 (b)). Then, the 2D rock block outlines are extracted using the proposed deep-learning-based method in section 2.1. After shape quantification and database establishment, 2D outlines with realistic shapes are employed to generate 3D rock block particles (Fig. 16). Based on the corresponding rock proportion and block gradation of each experimental specimen, the stochastic 3D specimens are reconstructed following the procedure proposed in section 2.2. Finally, the hybrid

models are obtained through the method provided in section 2.3. The reconstruction process of the hybrid model is illustrated in Fig. 16.

(a) Preparation of the heterogeneous specimens

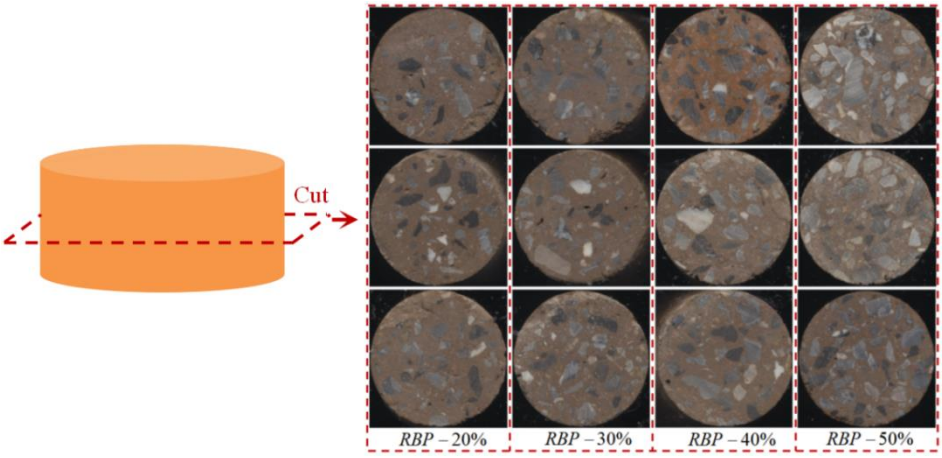

(b) Identify rock outlines from the middle planes of the specimens

Fig. 15 Preparation of the heterogeneous specimens and basic image data

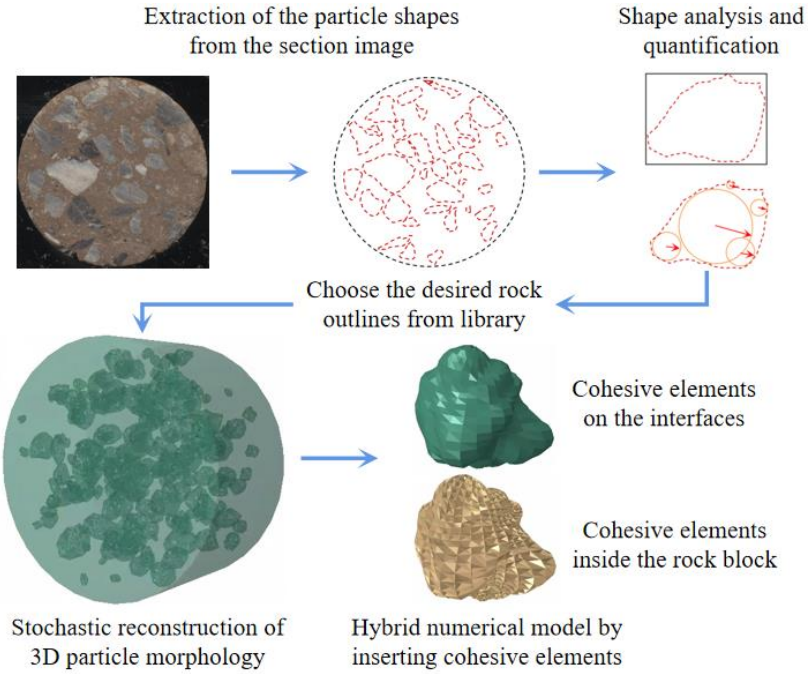

Fig. 66 The reconstruction process of the hybrid model

Then, the microparameters are determined following the calibration process mentioned in section

3.1. The calibrated macro-micro mechanical parameters of the 3D numerical model are summarised in Table. 3.

Table 3 Mechanical parameters of the numerical model

Mechanical parameters	Rocks (Poland cement)	Matrix (gypsum)	Cohesive elements		
			Matrix	Interface	Rocks
Elastic modulus/MPa	35000	6000	--	--	--
Poisson's ratio	0.22	0.3	--	--	--
Tensile stiffness (GPa/m)	--	--	3500	2000	25000
Shear stiffness (GPa/m)	--	--	800	750	8000
Normal traction criterion/MPa	--	--	1.5	0.8	3.5
Shear traction criterion/MPa	--	--	2.5	1.3	12
Mode-I fracture energy (N/m)	--	--	85	50	150
Mode-II-fracture energy (N/m)	--	--	140	90	300

3.2.2 Results of Brazilian tests and comparison

The experimental and numerical results of the split strength are compared herein. As shown in Fig. 17 (a) and Fig. 17 (b), the split strength of the experimental and that of numerical results shares a consistent ascendant trend with increasing BP. The increasing rate is notably improved when the rock proportion exceeds 30%. In addition, the dispersion of statistics slightly increases due to the improving heterogeneity introduced by the increase in the rock proportions. Additionally, as shown in Fig. 17 (c), the numerical results generally agree well with the experimental results, with a correlation coefficient of 0.92. Even though increasing the rock proportion can amplify the uncertainty in the prediction of split strength, the maximum error is within 8%. This suggests the validity of the proposed model.

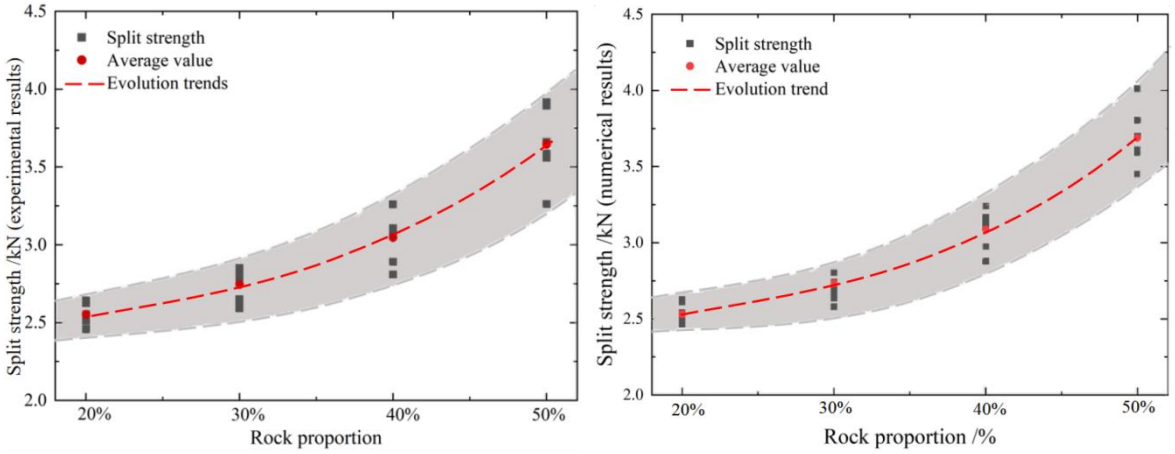

(a) Experimental results (b) Numerical results

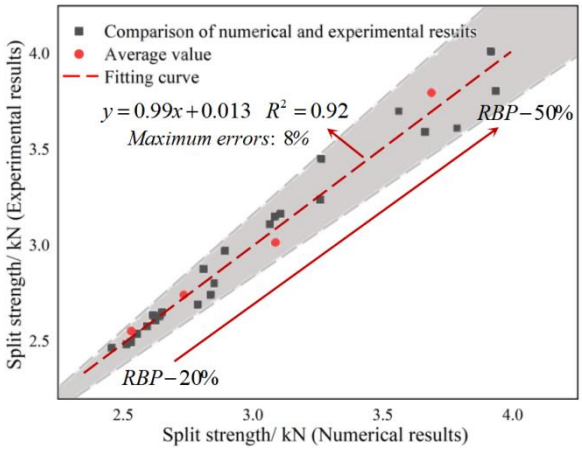

(c) Comparison of the numerical and experimental split strength results

Fig. 77 Numerical and experimental split strength results

The experimental and numerical split stiffness results are also compared. As shown in Fig. 18 (a) and Fig. 18 (b), both the experimental and numerical split stiffness results increase linearly with increasing rock proportion. Fig. 18 (c) shows the comparison results between the numerical and experimental results. The numerical results correspond well with the experimental results in general, with a correlation coefficient of 0.93. The maximum error of the split stiffness is within 6%. This proves the effectiveness of the proposed model from another aspect.

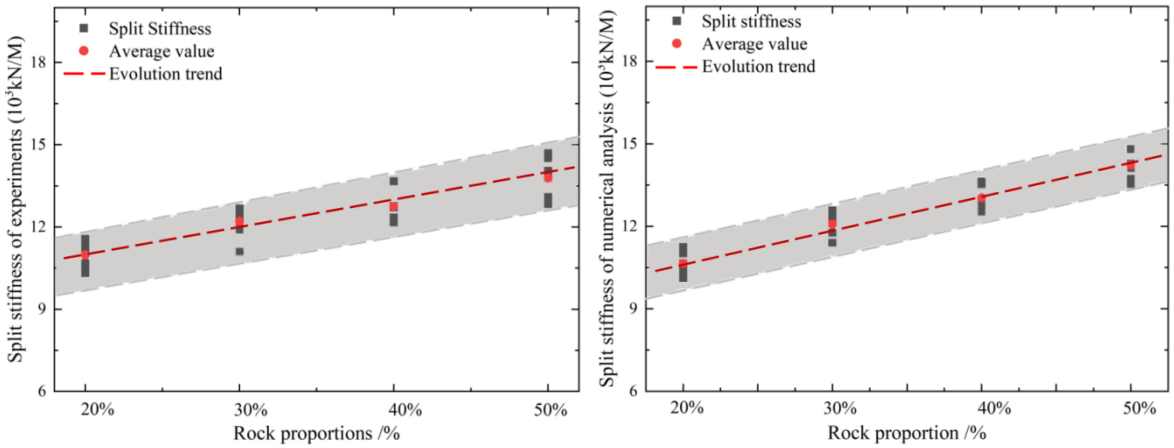

(a) Experimental results (b) Numerical results

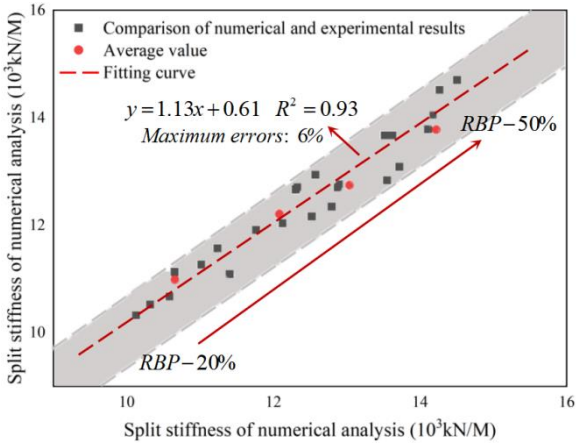

(c) Comparison of the numerical and experimental split stiffness results

Fig. 88 Numerical and experimental stiffness results

4 Discussion of influencing factors

To better understand the failure mechanism of heterogeneous geomaterials, this section illustrates applications of the proposed hybrid numerical method in analysing the influences of the interface strength and block-matrix strength ratio on the mechanical properties.

4.1 Influence of the strength ratio among rock blocks and matrix

To analyse the influences of the block-matrix strength ratio, realistic numerical specimens with various strength ratios are reproduced using the proposed method, while the tensile and shear strengths of cohesive elements in rock blocks are set to 80%, 120%, 160%, and 200% of those in the matrix. For all models, the mechanical properties of the cohesive elements on the interfaces remain the same.

(1) Failure characteristics

The failure evolution process of specimens with strength ratios of 200% and 80% are depicted in Fig 19. Cracks initiate from the interfaces among the block inclusions and matrix due to the relatively low interface strength, as shown in Fig 19. As block inclusions are much stronger than the matrix and their interfaces, cracks tend to develop along the interfaces and matrix rather than crossing the rock blocks, which results in a relatively irregular and tortuous failure path. With the development of cracks along the interfaces, a tensile crack then emerges at the tips of the interface cracks and penetrates vertically through the matrix. When the tensile split strength is reached, the stress shows a sharp drop from Point B to Point E, as shown in Fig. 19 (a). The descent trend shows some fluctuation, which may be caused by the friction and interlock effects of the block inclusions.

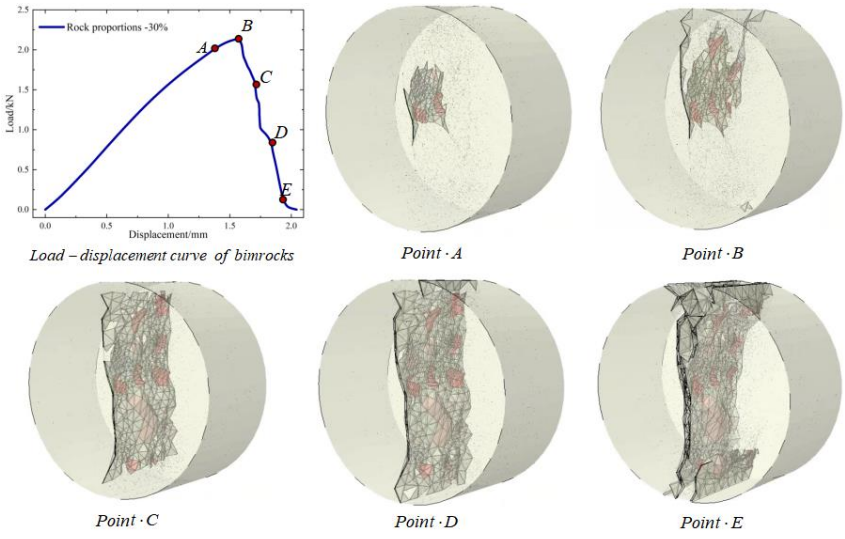

(a) Failure characteristics of specimens with strength ratios of 200%

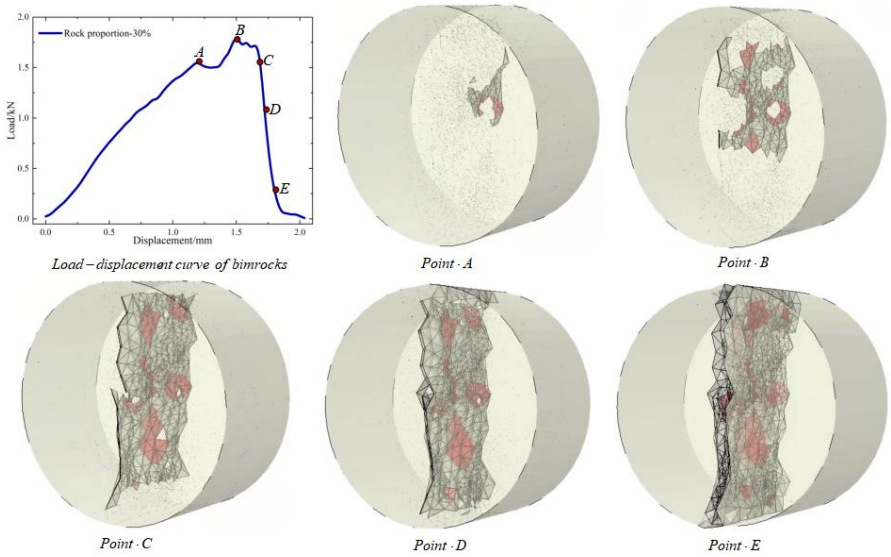

(b) Failure characteristics of specimens with the lowest strength ratio, i.e., 80%

Fig. 99 Failure evolution characteristics of specimens during the Brazil test

For the specimens with strength ratios of 80% depicted in Fig. 19 (b), the load-displacement curve exhibits obvious fluctuations during the peak strength regions, which may be caused by the splitting and failure of block inclusions. The failure paths are less tortuous than those illustrated in Fig. 19 (a), as the failure paths could directly pass through the soft block inclusions. After the tensile strength was reached, the cracks developed rapidly until the specimen was completely split apart. Furthermore, the stress shows a steep drop to zero. Thus, it is concluded that the strength ratio imposes a significant impact on the strength and failure pattern of heterogeneous geomaterials.

(2) Distribution of the split strength versus the strength ratio

It is widely accepted that the mechanical and failure properties may vary dramatically with different distributions of block inclusions along the cracking paths (Kalender et al., 2014,Wang et al., 2018 and Sharafisafa et al., 2020). To better understand the influence of the strength ratio on the mechanical properties, six different orientations (0°, 30°, 60°……150°) are tested for each specimen. Furthermore, four types of rock proportions ranging from 20% to 50% are considered. The split strength versus the strength ratio (80%, 120%, 160% and 200%) and the BPs are illustrated in Fig. 20.

In Fig. 20, the split strength generally grows with an increasing strength ratio. However, the increasing rate slows down after the strength ratio passes 160%. The reason for this result is that the split strength of heterogeneous geomaterials is largely dominated by the strength of the matrix and interfaces when the block inclusion is much stronger than the matrix.

Specifically, the evolution of the split strength versus the BPs shows an increasing trend when the strength ratio is larger than 100%. It can also be observed that the split strength increases notably when the rock proportion increases from 40% to 50%, which is consistent with the findings in

previous studies (Sonmez et al., 2004; Kalender et al., 2014 and Coli et al., 2020). Additionally, inspired by the conclusion in the existing work (Afifipour M et al., 2014; Kahraman et al., 2015), this phenomenon may be due to the interlock occurring among the hard inclusions, which could amplify the strengthening effects of rock blocks and impede the failure evolution. However, when the strength ratio is 80%, the split strength decreases as the BP increases from 20% to 50% because the block strength is weaker than the matrix strength in this situation. This phenomenon coincides with experimental results on the Misis fault breccia (Kahraman et al., 2015), which also has weak block inclusions.

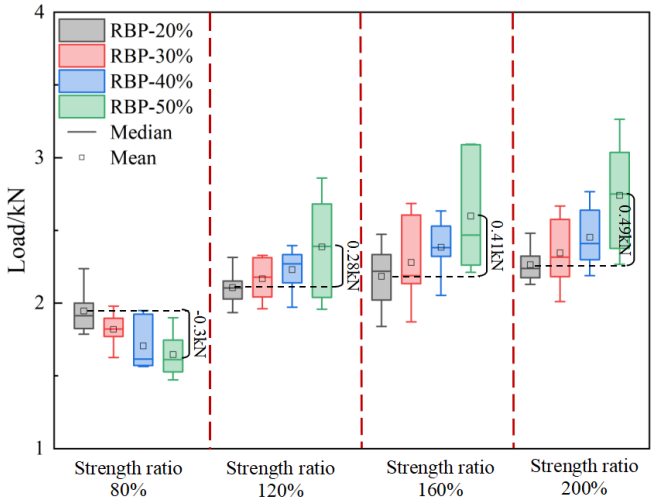

(a) Box plot of the split strength

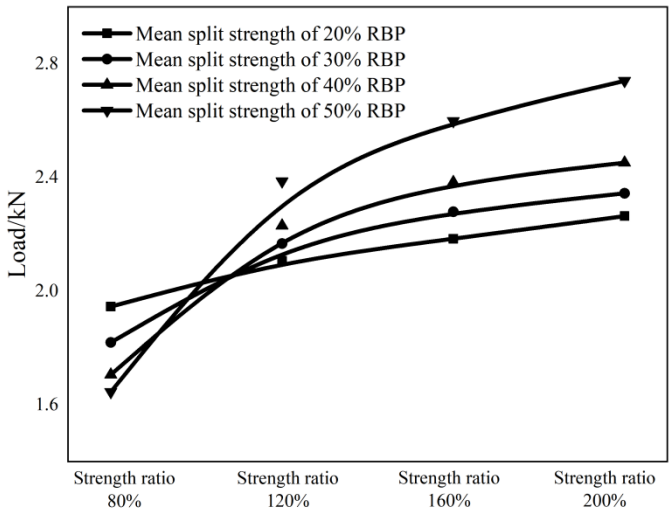

(b) Mean value of the split strength

Fig. 20 The evolution of the split strength versus the strength ratio under various BPs

4.2 Influence of the interface strength on heterogeneous geomaterials

According to the experimental results and the findings of previous studies (Li et al, 2013 and Zhu et al., 2020), the interface strength also plays an important role in determining the mechanical properties of block-containing materials. To further quantitatively evaluate the effects of the interface

strength on the split strength, two sets of numerical specimens with rock proportions of 20% and 50% are prepared. Each set consists of sixteen models with various interface strengths (40%, 80%, 120% and 160% of the matrix strength) and strength ratios (80%, 120%, 160% and 200% of the matrix strength). Each model is tested along six loading directions.

The relationships between the split strength and interface strength with various strength ratios are shown in Fig. 21. In Fig. 21, with increasing interface strength, general increasing trends of the split strengths for both sets are observed. The contribution of the strength ratio to the split strengths is clearly magnified with an increasing interface strength. Thus, it can be concluded that an increase in the interface strength will generally strengthen the heterogeneous geomaterials. By comparing Fig. 21 (b) and (d), the interface strength has profounder effects on the mechanical properties of heterogeneous rocks when the block proportion is 50%. It is inferred that the split strength is more sensitive to both the strength ratio and block proportion as the interface strength increases.

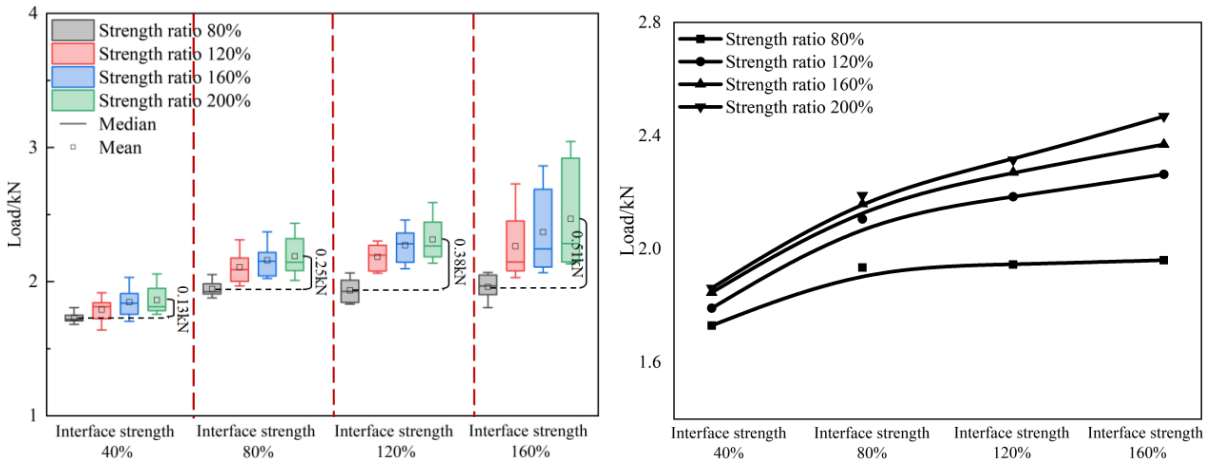

(a) Box chart of the split strength for a RBP of 20% (b) The mean split strength for a RBP of 20%

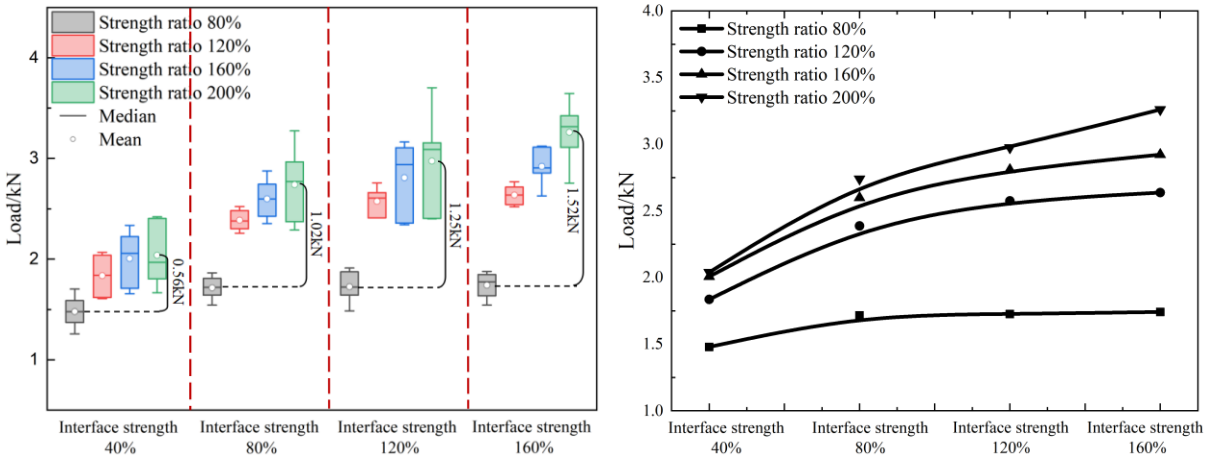

(c) Box chart of the split strength for a RBP of 50% (d) Mean split strength for a RBP of 50%

Fig. 21 Split strength evolution trend of specimens versus the interface strength

5 Conclusion

In this study, a hybrid computational approach was developed to model 3D realistic heterogeneous geomaterials considering 3D irregular block shapes, block-matrix interface characteristics and breakage of rock blocks. First, based on deep learning and computational geometry algorithms, numerical specimens with the quantitative control of the block shapes and size distribution can be reconstructed. Then, to capture the failure behaviours, a hybrid finite-discrete model was established by inserting cohesive elements into the meshed model. To validate the efficiency and accuracy of the proposed method from 2D to 3D, a series of physical and numerical Brazilian split tests were conducted on synthetic heterogeneous specimens. Finally, the effect of the strength ratio and interface strength on the mechanical and fracturing behaviour was systematically discussed. The conclusions drawn are as follows:

(1) The deep learning technique has been combined with computational geometry algorithms to automatically extract rock blocks from raw images to establish a database of 2D block outlines. On this basis, the 3D surface morphing approach and block allocation algorithm have been developed to reconstruct stochastic numerical models with the desired rock block geometry.

(2) The proposed hybrid finite-discrete approach with a set of calibrated parameters has been verified to effectively simulate the mechanical behaviour of block-containing materials. The numerical results agree well with the laboratory data for cases with different block proportions, and the failure characteristics of the numerical results also match well with the experimental observations with an evolution trend that is consistent as the block proportion increases.

(3) The block proportion was shown to have strong effects on the mechanical properties. Normally, the mechanical properties are improved by increasing the block proportion. However, the evolution trend will reverse if the rock is weaker than the matrix. Notably, owing to the interlock effects of rock blocks, the strength substantially increases when the rock proportion rises from 40% to 50% and the strength ratio is larger than 100%.

(4) A notable ascendant trend of the split strengths was found as the strength ratio or interface strength increased. Both strengthening effects can be amplified by increasing block proportion. However, the increasing rate tends to become moderate as the strength ratio or interface strength reaches their matrix value.

Regarding the good performance achieved, the proposed hybrid approach can serve as a promising tool for modelling the mechanical responses of heterogeneous strata with irregular inclusions during tunnelling and other geological engineering applications.

Acknowledgement

The financial support provided by the projects (grant No. 15209119, R5037-18F) from the Research Grants Council (RGC) of Hong Kong, Postdoctoral Science Foundation of China (2021M693681), National Natural Science Foundation of China (No. 51978677, 51708564), and the Foundation Research Project of China (Grant: JCKY2020110C096). This financial support is gratefully acknowledged.

Appendix: Description of 3D cohesive zone model

In the 3D cohesive zone model, the traction consists of a normal direction and two tangential directions across the crack surfaces. Fig. A1 shows a typical evolution law between the traction and crack separation in the normal and tangential directions, which is called the bilinear traction-separation model.

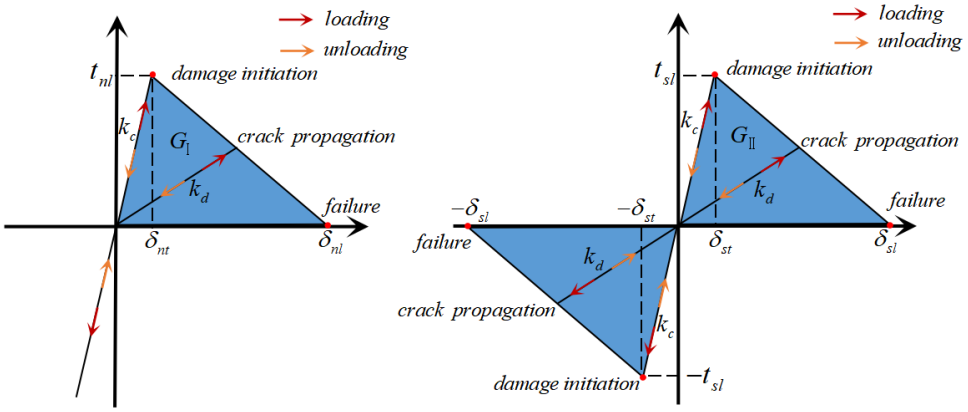

(a) Tensile behaviour (b) Shear behaviour.

Fig. A1 Constitutive model of the cohesive element

Owing to its simplicity and clarity, the bilinear traction-separation model is widely used and is considered an efficient and convenient model to capture material fracture behaviours. At the early stage, stress increases linearly with strain before damage initiation in both the normal and tangential directions, which can be expressed as follows (Su et al, 2010):

$$\sigma=\begin{Bmatrix}\sigma_n\\ \sigma_s\\ \sigma_t\end{Bmatrix}=\begin{bmatrix}E_{nn} & E_{ns} & E_{nt}\\ E_{ns} & E_{ss} & E_{st}\\ E_{nt} & E_{st} & E_{tt}\end{bmatrix}\begin{Bmatrix}\varepsilon_n\\ \varepsilon_s\\ \varepsilon_t\end{Bmatrix}=\frac{1}{T_0}\begin{bmatrix}E_{nn} & E_{ns} & E_{nt}\\ E_{ns} & E_{ss} & E_{st}\\ E_{nt} & E_{st} & E_{tt}\end{bmatrix}\begin{Bmatrix}\delta_n\\ \delta_s\\ \delta_t\end{Bmatrix}=\begin{bmatrix}k_{nn} & k_{ns} & k_{nt}\\ k_{ns} & k_{ss} & k_{st}\\ k_{nt} & k_{st} & k_{tt}\end{bmatrix}\begin{Bmatrix}\delta_n\\ \delta_s\\ \delta_t\end{Bmatrix} \quad \text{(A1)}$$

where σ is the nominal traction vector, ε is the nominal strain vector, and δ is a displacement vector that consists of three components in 3D scenarios. E and k are the elastic modulus and stiffness matrix, respectively. T_0 is the original thickness of the cohesive element.

Then, with deformation growth, the curves enter a softening stage where damage is initiated. In this study, the damage initiation law is determined by quadratic nominal stress, which takes into account the interaction of three traction components, as shown in Fig. A2.

$$\left\{\frac{\langle t_n \rangle}{t_{nl}}\right\}^2 + \left\{\frac{t_s}{t_{sl}}\right\}^2 + \left\{\frac{t_t}{t_{tl}}\right\}^2 = 1 \tag{A2}$$

where t_{nl}, t_{sl} and t_{tl} represent the peak strength of the nominal stress when the deformation is either purely normal to the interface or purely parallel to the first and second shear directions. t_n, t_s and t_t are stress components. The operator $\langle\ \rangle$ is the Macauley operator defined as $\langle x \rangle = \frac{1}{2}(x + |x|)$.

After damage initiation, the mechanical properties of the material tend to degrade gradually upon loading. To define the damage evolution law of stiffness, a scalar damage variable D is employed to represent the overall damage of the interfaces, with which the penalty tensile and shear stiffness can be expressed as follows:

$$k_{np} = (1-D)k_n\ ;\ k_{sp} = (1-D)k_s\ ;\ k_{tp} = (1-D)k_t\ ; \tag{A3}$$

For the linear softening stage, as shown in Fig. A1, the damage variable can be expressed as follows:

$$D = \frac{\delta_{mf}(\delta_{mm} - \delta_{mo})}{\delta_{mm}(\delta_{mf} - \delta_{mo})} \tag{A4}$$

where δ_{mm} represents the maximum displacement during the loading process, and δ_{mo} and δ_{mf} are the effective relative displacements at the damage initiation state and final failure state, respectively. The effective relative displacement is defined as follows:

$$\delta_m = \sqrt{\langle \delta_n \rangle^2 + \delta_s^2 + \delta_t^2} \tag{A5}$$

The mixed-mode softening law can be illustrated in a single 3D map by representing the tensile mode and shear mode on the perpendicular planes, as shown in Fig. A2.

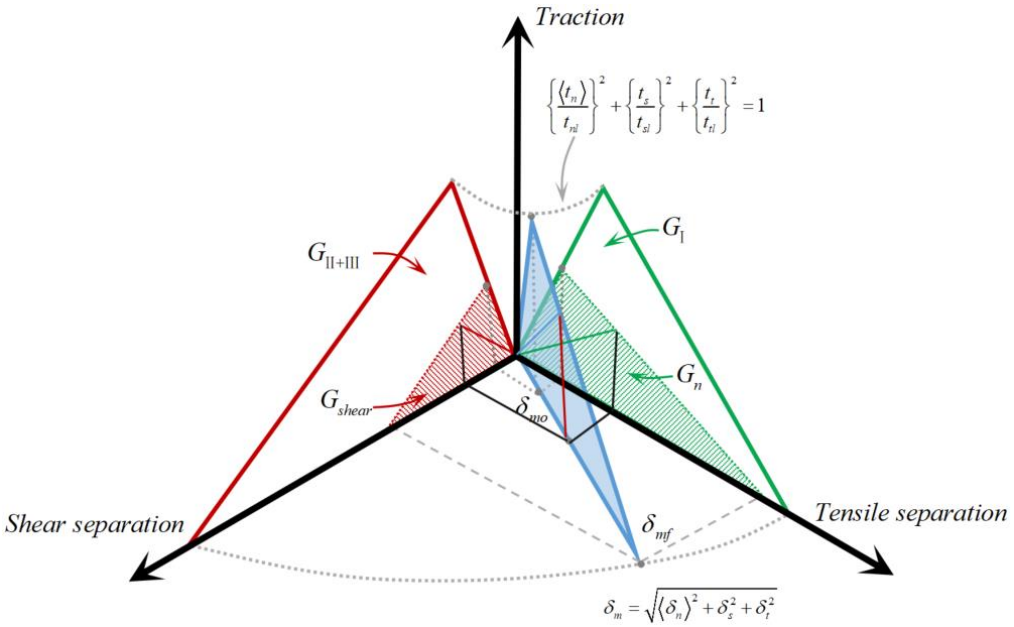

Fig. A2 Traction-separation response of the cohesive element in mixed mode

References:

Afifipour M., Moarefvand P., 2014. Mechanical behavior of bimrocks having high rock block proportion. International Journal of Rock Mechanics & Mining Sciences, 65, 40-48.

Barenblatt G.I., 1959. The formation of equilibrium cracks during brittle fracture general ideas and hypotheses axially-symmetric cracks. J.appl.math.mech, 23(3), 622-636.

Coli N., Berry P., Boldini D., et al., 2012. The contribution of geostatistics to the characterisation of some bimrock properties. Engineering Geology, 137-138 (7), 53-63.

Dugdale, D.S., 1960. Yielding of steel sheets containing slits. Journal of Mechanics of Physics and Solids 8, 100-104.

E. Medley, et al., 2011. Geopractitioner approaches to working with antisocial mélanges［C］// /WAKABAYASHI J, DILEK Y．Mélanges: Processes of Formation and Societal Significance. Geological Society of America, 261-277.

E. Medley., 2002. Estimating block size distributions of mélanges andsimilar block-in matrix rocks (bimrocks), in: R. Hammah, Curran J. BawdenW, Telesnicki (Eds.), Proceedings of 5th North AmericanRock Mechanics Symposium (NARMS), University of Toronto Press, Toronto, Canada, pp. 509–606.

E. Medley., 1994. The Engineering Characterization of Melanges and Similar Block-inMatrix Rocks (bimrocks) (Ph.D.), University of Califronia, Berkeley.

E.S. Lindquist, R.E. Goodman., 1994. Strength and deformation properties of a physical model melange, 1st North American Rock Mechanics Symposium, American Rock Mechanics Association.

Emad K., Mehdi A., et al., 2019. Statistical analysis of bimslope stability using physical and numerical models. Engineering Geology, 254: 13-24.

Fonseca, J., O'Sullivan, C., Coop, M.R., Lee,P.D., 2012. Non-invasive characterization of particle morphology of natural sands. Soils & Foundations, 52(4), 712-722.

Farsi A., Xiang J., Latham JP., et al., 2021. Packing simulations of complex-shaped rigid particles using FDEM: An application to catalyst pellets. Powder Technology. 380: 443-461.

Gong J., Liu J., Liang C., 2019. Shear behaviors of granular mixtures of gravel-shaped coarse and spherical fine particles investigated via discrete element method, Powder Technology, 353, 178-194.

Jin YF, Yin Z-Y, Zhou WH, Horpibulsuk S (2019). Identifying parameters of advanced soil models using an enhanced Transitional Markov chain Monte Carlo method. Acta Geotech., 14(6), 1925-1947.

Jin YF, Yin Z-Y, Zhou WF, Liu X (2020). Intelligent model selection with updating parameters during staged excavation using optimization method. Acta Geotech., 15(9), 2473-2491.

Jiang H.X., Meng D., 2018. 3D numerical modelling of rock fracture with a hybrid finite and cohesive element method. Engineering Fracture Mechanics, 199: 280-293.

Joseph K Anochie-Boateng, Julius J. Komba et al., 2013. Three-dimensional laser scanning technique to quantify aggregate and ballast shape properties. Construction & Building Materials, 43(6), 389-398.

Kahraman S., Alber M., M. Fener., O. Gunaydin., 2015. An assessment on the indirect determination of the volumetric block proportion of Misis fault breccia (Adana, Turkey). Bulletin of Engineering Geology and the Environment, 74(3):899-907.

Kalender A., Sonmez H., et al., 2014. An approach to predicting the overall strengths of unwelded

751 bimrocks and bimsoils. Engineering Geology, 183, 65-79.
752 Lai Z, Chen Q., 2019. Reconstructing granular particles from X-ray computed tomography using the TWS
753 machine learning tool and the level set method. Acta Geotechnica, 14(1), 1-18.
754 Li X, Zhao J., 2019. An overview of particle-based numerical manifold method and its application to
755 dynamic rock fracturing. Journal of Rock Mechanics and Geotechnical Engineering, 11(3), 684-700.
756 Li Y., 2013. Effects of particle shape and size distribution on the shear strength behavior of composite soils.
757 Bulletin of Engineering Geology & the Environment, 72(3-4), 371-381.
758 Li Z. Q., Hu F.H., Qi S.W., Hu R.L., 2020. Strain-softening failure mode after the post-peak as a unique
759 mechanism of ruptures in a frozen soil-rock mixture, Engineering Geology, 274, 105725.
760 Liang Z.Y., Nie Z.H., An A.J., et al., 2019. A particle shape extraction and evaluation method using a deep
761 convolutional neural network and digital image processing, Powder Technology, 353, 156-170.
762 Mollon G., Zhao J., 2013. Generating realistic 3D sand particles using Fourier descriptors. Granular Matter,
763 15(1), 95-108.
764 Munjiza A., Owen D R J., Bicanic N, 1995. A combined finite‐discrete element method in transient
765 dynamics of fracturing solids[J]. Engineering computations. 12: 145-174.
766 Munjiza A., 2004. The combined finite-discrete element method[M]. John Wiley & Sons.
767 Morris J P., Rubin M B., Block G I., et al., 2006. Simulations of fracture and fragmentation of geologic
768 materials using combined FEM/DEM analysis. International Journal of Impact Engineering 33(1-12):
769 463-473.
770 Mahabadi OK., Lisjak A., Munjiza A., et al., 2012. Y-Geo: new combined finite-discrete element
771 numerical code for geomechanical applications. International Journal of Geomechanics 12(6): 676-688.
772 Nguyen V.P., 2014. An open source program to generate zero-thickness cohesive interface elements.
773 Advances in Engineering Software, 2014, 74(8), 27-39.
774 Napoli M.L., Barbero M, Ravera E, et al., 2018. A stochastic approach to slope stability analysis in
775 bimrocks. International Journal of Rock Mechanics and Mining sciences, 101, 41-49.
776 Nie Z.H., Fang C., Gong J., et al., 2020. DEM study on the effect of roundness on the shear behaviour of
777 granular materials. Computers and Geotechnics, 352, 314-324.
778 Nie Z.H., Fang C., Gong J., et al., 2020. Exploring the effect of particle shape caused by erosion on the
779 shear behaviour of granular materials via the DEM. International Journal of Solids and Structures, 202,
780 1-11.
781 Nie Z.H., Liang Z.Y., Wang X., 2018. A three-dimensional particle roundness evaluation method. Granular
782 Matter, 20(2), 20-32.
783 Nie Z.H., Liang Z.Y., Wang X., et al., 2018. Evaluation of granular particle roundness using digital image
784 processing and computational geometry. Construction and Building Materials, 172, 319-329.
785 Nie Z.H., Wang X., Liang Z.Y. et al., 2018. Quantitative analysis of the three-dimensional roundness of
786 granular particles, Powder Technology, 336, 584-593,
787 R. Belda, M. Palomar, J.L. Peris-Serra, et al., 2020. Compression failure characterization of cancellous
788 bone combining experimental testing, digital image correlation and finite element modeling, International
789 Journal of Mechanical Sciences, 165, 105213
790 Raymond, L.A., 1984. Classification of melanges. In: Raymond, L.A., Boulder, L.A. (Eds.), Melanges:
791 Their Nature, Origin and Significance. Geol. Soc. of America, pp 7-20.

792 Sun L., Liu Q., Grasselli G., et al., 2020. Simulation of thermal cracking in anisotropic shale formations
793 using the combined finite-discrete element method. Comput Geotech. 117: 103237.
794 Su D., Wang X., 2020. Characterization and regeneration of 2D general-shape particles by a Fourier
795 series-based approach, Construction and Building Materials,Volume 250, 118806.
796 Shao J.F., Xie S.Y., Gilles D., et al., 2017. Anisotropic poroplasticity in saturated porous media, effect of
797 confining pressure, and elevated temperature. Porous Rock Fracture Mechanics, pp 27-46.
798 Sharafisafa, M., Aliabadian, Z., Shen, L., 2020. Crack initiation and failure development in bimrocks using
799 digital image correlation under dynamic load. Theoretical and Applied Fracture Mechanics, 109(5),
800 102688.
801 Sharafisafa M., Aliabadian Z., Shen, L., 2020. Crack initiation and failure of block-in-matrix rocks under
802 Brazilian test using digital image correlation. Theoretical and Applied Fracture Mechanics, 109(10),
803 102743.
804 Sonmez H., Tuncay E., Gokceoglu C., 2004. Models to predict the uniaxial compressive strength and the
805 modulus of elasticity for ankara agglomerate. International Journal of Rock Mechanics & Mining Sciences,
806 41(5), 717-729.
807 Sonmez H., Ercanoglu M., Kalender A., et al., 2016. Predicting uniaxial compressive strength and
808 deformation modulus of volcanic bimrock considering engineering dimension. International Journal of
809 Rock Mechanics & Mining Sciences, 86, 91-103.
810 Sonmez H., Gokceoglu C., Medley E. et al., 2006. Estimating the uniaxial compressive strength of a
811 volcanic bimrock[J]. International Journal of Rock Mechanics and Mining Sciences, 43(4), 554-561.
812 Su X.T., Yang Z.J., Liu G.H., 2009. Monte Carlo simulation of complex cohesive fracture in random
813 heterogeneous quasi-brittle materials. International Journal of Solids and Structures, 47(17), 2336-2345.
814 Su X., Yang, Z., Liu G., 2010. Finite Element Modelling of Complex 3D Static and Dynamic Crack
815 Propagation by Embedding Cohesive Elements in Abaqus. Acta Mechanica Solida Sinica, 23(3), 271-282.
816 Sulaiman, H.A., Bade, A., Abdullah, M. H., 2014. Computing distance using internal axis-aligned
817 bounding-box for nearly intersected objects. AIP Conference Proceedings. 1602(1), 343-349.
818 Tatone B., Grasselli G., 2015. A calibration procedure for two-dimensional laboratory-scale hybrid
819 finite-discrete element simulations. International Journal of Rock Mechanics and Mining Sciences, 75,
820 56-72.
821 Wei D H., Zhao B D., D Dias-da-Costa., et al., 2019 An FDEM study of particle breakage under rotational
822 point loading. Engineering Fracture Mechanics, 330, 221-237.
823 Wang Y., Li X., 2015. Experimental study on cracking damage characteristics of a soil and rock mixture by
824 upv testing. Bulletin of Engineering Geology & the Environment, 74(3), 775-788.
825 Wang X., Tian K., Su, D., Zhao, J., 2019. Superellipsoid-based study on reproducing 3d particle geometry
826 from 2d projections. Computers and Geotechnics, 114(10), 103131.1-103131.15.
827 Wang X., Liang Z.Y., Nie Z.H. et al., 2019. Stochastic numerical model of stone-based materials with
828 realistic stone-inclusion features. Construction and Building Materials, 197, 830-848.
829 Wang Y., Li C.H, Hu Y.Z., 2018. 3d image visualization of meso-structural changes in a bimsoil under
830 uniaxial compression using x-ray computed tomography (ct). Engineering Geology, 248, 61-69.
831 Wang Y., Que J.M., Wang C et al., 2018. Three-dimensional observations of mesostructural changes in
832 bimsoil using X-ray computed tomography (CT) under triaxial compression, Constr. Build. Mater, 190 ,

773-786.
Wu Z., Xu X., Liu Q., et al., 2018. A zero-thickness cohesive element-based numerical manifold method for rock mechanical behaviour with micro-Voronoi grains. Engineering Analysis with Boundary Elements, 96, 94-108.
Xu W.J., Yue Z.Q., Hu R.L., 2008. Study on the mesostructure and mesomechanical characteristics of the soil-rock mixture using digital image processing based finite element method. International Journal of Rock Mechanics & Mining ences, 45(5), 749-762.
Xu W.J., Zhang H.Y., Jie Y.X., et al., 2015. Generation of 3D random meso-structure of soil-rock mixture and its meso-structural mechanics based on numerical tests. Journal of Central South University, 22(02), 619-630.
Xu W.J., Wang S., Zhang H.Y., Zhang Z.L., 2016. Discrete element modelling of a soil-rock mixture used in an embankment dam. International Journal of Rock Mechanics and Mining Sciences. 86, 141-156.
Xu, Y.F., 2018. The fractal evolution of particle fragmentation under different fracture energy. Powder Technology An International Journal on the Science & Technology of Wet & Dry Particulate Systems, 323, 337-345.
Yin Z-Y, Jin YF, Shen SL, Huang HW (2017). An efficient optimization method for identifying parameters of soft structured clay by an enhanced genetic algorithm and elastic-viscoplastic model. Acta Geotech., 12(4): 849–867.
Yin Z-Y, Jin YF, Shen JS, Hicher PY (2018). Optimization techniques for identifying soil parameters in geotechnical engineering: Comparative study and enhancement. Int. J. Numer. Anal. Methods Geomech., 42(1):70-94.
Yan C., Jiao Y., Zheng H., 2019. A three-dimensional heat transfer and thermal cracking model considering the effect of cracks on heat transfer. International Journal for Numerical and Analytical Methods in Geomechanics. 43(10):1825- 1853.
Yan C., Zheng H., Huang D et al, 2021. A coupled contact heat transfer and thermal cracking model for discontinuous and granular media. Computer Methods in Applied Mechanics and Engineering, 375: 113587.
Zhao B., Wang J., Coop M.R., et al, 2015. An investigation of single sand particle fracture using x-ray micro-tomography. Géotechnique, 65(8), 625-641.
Zhou B., Wang J., Zhao B., 2015. Micromorphology characterization and reconstruction of sand particles using micro X-ray tomography and Spherical harmonics. Engineering Geology, 184, 126-137.
Zhou B., Wang J., 2015. Random generation of natural sand assembly using micro X-ray tomography and Spherical harmonics. Géotechnique Letters, 5, 6-11.
Zhou B., Wei D., Quan K., et al., 2020. Study on the effect of particle morphology on single particle breakage using a combined finite-discrete element method. Computers and Geotechnics, 122, 103532.
Zhu Y.G, Gong J, Nie Z.H., 2020. Shear behaviours of cohesionless mixed soils using the DEM: The influence of coarse particle shape[J]. Particuology, 55(04), 151-165.

871 # Figure captions:

872